A&A 606, A55 (2017)
DOI: 10.1051/0004-6361/201731272

Astronomy & Astrophysics

Rotational mixing in carbon-enhanced metal-poor stars with *s*-process enrichment⋆

E. Matrozis⋆⋆ and R. J. Stancliffe

Argelander-Institut für Astronomie (AIfA), University of Bonn, Auf dem Hügel 71, 53121 Bonn, Germany
e-mail: elvijs@astro.uni-bonn.de

Received 30 May 2017 / Accepted 23 July 2017

ABSTRACT

Carbon-enhanced metal-poor (CEMP) stars with *s*-process enrichment (CEMP-*s*) are believed to be the products of mass transfer from an asymptotic giant branch (AGB) companion, which has long since become a white dwarf. The surface abundances of CEMP-*s* stars are thus commonly assumed to reflect the nucleosynthesis output of the first AGB stars. We have previously shown that, for this to be the case, some physical mechanism must counter atomic diffusion (gravitational settling and radiative levitation) in these nearly fully radiative stars, which otherwise leads to surface abundance anomalies clearly inconsistent with observations. Here we take into account angular momentum accretion by these stars. We compute in detail the evolution of typical CEMP-*s* stars from the zero-age main sequence, through the mass accretion, and up the red giant branch for a wide range of specific angular momentum j_a of the accreted material, corresponding to surface rotation velocities, v_{rot}, between about 0.3 and 300 km s^{-1}. We find that only for $j_a \gtrsim 10^{17}$ cm^2 s^{-1} ($v_{rot} > 20$ km s^{-1}, depending on mass accreted) angular momentum accretion directly causes chemical dilution of the accreted material. This could nevertheless be relevant to CEMP-*s* stars, which are observed to rotate more slowly, if they undergo continuous angular momentum loss akin to solar-like stars. In models with rotation velocities characteristic of CEMP-*s* stars, rotational mixing primarily serves to inhibit atomic diffusion, such that the maximal surface abundance variations (with respect to the composition of the accreted material) prior to first dredge-up remain within about 0.4 dex without thermohaline mixing or about 0.5–1.5 dex with thermohaline mixing. Even in models with the lowest rotation velocities ($v_{rot} \lesssim 1$ km s^{-1}), rotational mixing is able to severely inhibit atomic diffusion, compared to non-rotating models. We thus conclude that it offers a natural solution to the problem posed by atomic diffusion and cannot be neglected in models of CEMP-*s* stars.

Key words. stars: carbon – stars: evolution – stars: abundances – stars: rotation – binaries: general

1. Introduction

The tireless hunt for the most metal-poor and thus oldest stars in the Galaxy (e.g. Beers et al. 1985; Christlieb et al. 2001; Yanny et al. 2009; Ahn et al. 2014) has revealed that a significant fraction of metal-poor stars are highly enriched in carbon compared to the Sun. While these carbon-enhanced metal-poor (CEMP) stars ([C/Fe] $\gtrsim$ 1; Beers & Christlieb 2005; Masseron et al. 2010) make up only about 10% of all stars at [Fe/H] $\simeq -2$[1], their prevalence rapidly increases towards lower metallicities to near 100% by [Fe/H] $\simeq -4$ (Lucatello et al. 2006; Carollo et al. 2012; Yong et al. 2013; Lee et al. 2013; Placco et al. 2014). Spectroscopic studies have subsequently shown that CEMP stars are also commonly marked by large abundances of elements produced by the slow (*s*) and/or rapid (*r*) neutron-capture process, such as barium and europium. Accordingly, CEMP stars are further classified into CEMP-*s*, CEMP-*r*, and CEMP-*r*/*s* stars (Beers & Christlieb 2005; Masseron et al. 2010).

Many of these CEMP stars are relatively unevolved, being located on the main sequence or on the red giant branch. The prodigious amounts of carbon and heavy elements observed in these stars are thus expected to have external origins. Moreover, given the very different conditions required for the *s*- and *r*-process to operate – neutron densities of $n \lesssim 10^7$ cm^{-3} (Busso et al. 1999) and $n \gtrsim 10^{20}$ cm^{-3} (Wehmeyer et al. 2015), respectively – the different sub-classes most likely have distinct formation sites. A key insight into the origin of CEMP-*s* stars ([Ba/Fe] > 1 and [Ba/Eu] > 0; Masseron et al. 2010) comes from their radial motion. Many studies over the years have shown that the radial velocity of these objects periodically varies, indicating the presence of an unseen companion (Lucatello et al. 2005; Starkenburg et al. 2014; Hansen et al. 2016). The current view on the origin of these stars is thus accretion of carbon- and *s*-process-rich material from an asymptotic giant branch (AGB) companion that has since become a white dwarf and faded from view. This makes CEMP-*s* stars the low-metallicity analogs of Ba stars and CH stars (McClure & Woodsworth 1990; Jorissen et al. 2016).

Carbon-enhanced metal-poor stars with *s*-process enrichment thus provide a window onto the nucleosynthesis of the earliest generations of low-mass AGB stars, an important contributor to the chemical evolution of the Universe (e.g. Travaglio et al. 1999, 2001; Kobayashi et al. 2011; Bisterzo et al. 2014). To reliably link the surface abundances of CEMP-*s* stars with the nucleosynthesis output of these long-extinct AGB stars, however, we must understand what happens to the material after it is accreted by the less evolved

⋆ A quantitative summary of the models presented in this paper (mainly the stellar properties and surface abundances at key points of the evolution) is only available at the CDS via anonymous ftp to cdsarc.u-strasbg.fr (130.79.128.5) or via http://cdsarc.u-strasbg.fr/viz-bin/qcat?J/A+A/606/A55

⋆⋆ Member of the International Max Planck Research School (IMPRS) for Astronomy and Astrophysics at the Universities of Bonn and Cologne.

[1] The relative abundance of element A with respect to element B is [A/B] = $\log(C_A/C_B) - \log(C_A/C_B)_\odot$ where C is the number or mass fraction.

companion. In particular, will it simply remain on the surface, or mix with the material below? And if it does mix, are all elements affected similarly, or is the nucleosynthesis signature of the accreted material altered such that the surface abundances no longer reflect the accreted composition?

Most studies that aim at linking the abundances of CEMP-*s* stars to low-metallicity AGB nucleosynthesis models allow for some overall dilution of the accreted matter in the original material of the star (e.g. Bisterzo et al. 2011, 2012; Abate et al. 2015a,b). While this approach works rather well in many cases, in a previous paper we showed that the competition between gravitational settling and radiative levitation should considerably modify the surface abundances of CEMP-*s* stars, in particular distorting the abundance ratios between different elements, and concluded that either relatively high mass loss or some additional mixing is required to bring the models in accord with observations (Matrozis & Stancliffe 2016).

We remained agnostic as to the cause of this extra mixing. But rotational mixing is a promising candidate, since the accreted material should carry with it some angular momentum. In fact, the angular momentum content may be so high that an interesting question is how the accreting star can deal with it and accrete more than a few hundredths of a solar mass of material (Matrozis et al. 2017). Here we sidestep that issue and simply assume that the newly accreted layers of CEMP-*s* stars, which can have masses up to some tenths of a solar mass, are spinning more rapidly than their interiors. We then follow the post-mass-transfer evolution of these stars, in particular noting the evolution of their surface abundances as a result of rotational mixing, combined with atomic diffusion and thermohaline mixing.

2. Methods

We use a version of the STARS code (Eggleton 1971, 1972; Pols et al. 1995; Stancliffe & Eldridge 2009) to produce all the models presented here. The modifications introduced for modelling rotating stars are described in Potter et al. (2012b,a). In particular, the internal transport of specific angular momentum $j \propto \Omega r^2$ is modelled by a diffusion equation following Heger et al. (2000):

$$\frac{\mathrm{d}\left(\Omega r^2\right)}{\mathrm{d}t} = \frac{\partial}{\partial m}\left[\left(4\pi r^2 \rho\right)^2 r^2 \left(D_{\mathrm{conv}} + D_{\mathrm{rot}}\right) \frac{\partial \Omega}{\partial m}\right]. \quad (1)$$

Here Ω is the angular velocity; t is time; r and m are the radial and mass coordinate, respectively; ρ is the density; D_{conv} is the convective mixing coefficient (given by mixing length theory; Böhm-Vitense 1958, we set $\alpha_{\mathrm{MLT}} = 2$); and D_{rot} is the turbulent viscosity given by:

$$D_{\mathrm{rot}} = D_{\mathrm{ES}} + D_{\mathrm{DSI}} + D_{\mathrm{SSI}} + D_{\mathrm{SHI}} + D_{\mathrm{GSF}}. \quad (2)$$

In this equation each individual term corresponds to turbulent transport arising from, respectively, Eddington-Sweet (ES) circulation (Kippenhahn 1974), dynamical and secular shear instabilities (Zahn 1974; Endal & Sofia 1978), the Solberg-Høiland instability (Wasiutynski 1946), and the GSF instability (Goldreich & Schubert 1967; Fricke 1968). We refer the reader to Heger et al. (2000) for a discussion of the origin and evaluation of each of these terms.

The mass fraction X_i of each species i evolves according to

$$\frac{\mathrm{d}X_i}{\mathrm{d}t} = \frac{\partial}{\partial m}\left[\left(4\pi r^2 \rho\right)^2 D_{\mathrm{mix},i} \frac{\partial X_i}{\partial m}\right] - \frac{\partial}{\partial m}\left(4\pi r^2 \rho X_i w_i\right) + R_i. \quad (3)$$

Here R_i accounts for nuclear reactions, w_i is the atomic diffusion velocity as described in Matrozis & Stancliffe (2016), and $D_{\mathrm{mix},i}$ in general is given by

$$D_{\mathrm{mix},i} = D_{\mathrm{conv}} + D_{\mu} + D_i + f_{\mathrm{c}} D_{\mathrm{rot}}, \quad (4)$$

where D_{μ} and D_i are the thermohaline mixing (Denissenkov 2010) and concentration diffusion coefficients, respectively.

There are two adjustable parameters in our adopted prescription for rotational mixing. First, the parameter f_{c} in Eq. (4) determines the contribution of the rotationally induced instabilities to chemical transport. Second, many of the terms in Eq. (2) depend on the molecular weight gradient ∇_{μ}. The sensitivity of rotational mixing to μ-gradients is assumed to be reduced by a factor f_{μ}, i.e. ∇_{μ} is replaced by $f_{\mu}\nabla_{\mu}$. Following Heger et al. (2000) we adopt $f_{\mathrm{c}} = 1/30$ (Chaboyer & Zahn 1992) and $f_{\mu} = 0.05$. The influence of these parameters is examined in Sect. 4.3.

To save a considerable amount of computational time, we do not use the OP opacities and radiative accelerations (Badnell et al. 2005; Seaton 2007) introduced in the code by Matrozis & Stancliffe (2016). Instead we use the OPAL-based (Iglesias & Rogers 1996) opacity tables of Eldridge & Tout (2004) and ignore radiative levitation for now. This is perfectly sufficient to get a handle on the importance of atomic diffusion in a given model.

As in related earlier work (Stancliffe et al. 2007; Stancliffe & Glebbeek 2008; Matrozis & Stancliffe 2016), accretion of material is simulated by increasing the mass of the models at a rate of $10^{-6}\ M_{\odot}\ \mathrm{yr}^{-1}$. The composition of the added mass is set to the average composition of the AGB models of Lugaro et al. (2012). In particular, we use the yields from their models with initial masses $M_1 = 0.9$, 1.0, 1.25 and 1.5 $M_{\odot}$. The age, at which mass accretion starts is $t_{\mathrm{mt}} = 9.1$, 6.3, 3.06, and 1.8 Gyr, respectively (see Table 1 in Matrozis & Stancliffe 2016). All models have a zero-age main sequence (ZAMS) metallicity of $Z = 10^{-4}$ (Asplund et al. 2009, scaled to [Fe/H] = −2.14).

We adopt the same grid as in Matrozis & Stancliffe (2016): the initial secondary masses are $M_{2,\mathrm{i}} = 0.6$–$0.8\ M_{\odot}$ in steps of $0.05\ M_{\odot}$, and the accreted masses span $\Delta M = 0.05$–$0.3\ M_{\odot}$ (with some $M_{2,\mathrm{i}} = 0.8\ M_{\odot}$ models with $\Delta M = 10^{-3}, 10^{-2}\ M_{\odot}$), resulting in final CEMP star masses $M_{2,\mathrm{f}} = 0.8$–$0.95\ M_{\odot}$ (Abate et al. 2015c). For each combination of M_1, $M_{2,\mathrm{i}}$ and ΔM we have one more dimension: the specific angular momentum j_{a} of the added material. We investigate ten values of j_{a} in the range $(0.001$–$1) \times 10^{18}\ \mathrm{cm}^2\ \mathrm{s}^{-1}$. While the specific angular momentum of the accreted material in real systems is likely closer to the higher end of these values (Sect. 4.1), this range can be interpreted as representing different degrees of angular momentum loss during accretion and is suitable to produce CEMP-*s* models with surface rotation velocities between $v_{\mathrm{rot}} \lesssim 0.5\ \mathrm{km\,s}^{-1}$ (i.e. nearly stationary) and $v_{\mathrm{rot}} \gtrsim 300\ \mathrm{km\,s}^{-1}$ (close to critical rotation), once they have settled on the post-mass-transfer main sequence. On the ZAMS the models are uniformly rotating with a surface rotation velocity $v_{\mathrm{rot}} \simeq 0.3\ \mathrm{km\,s}^{-1}$.

3. Results

Prior to summarizing the general features of our calculations (Sect. 3.3), we consider in depth the evolution of a system characterized by $M_1 = 1.25\ M_{\odot}$, $M_{2,\mathrm{i}} = 0.75\ M_{\odot}$, $\Delta M = 0.05\ M_{\odot}$, first under the influence of rotational mixing alone (Sect. 3.1), and then together with diffusion and thermohaline mixing (Sect. 3.2).

3.1. Models with rotational mixing only

Figure 1 shows the Hertzsprung-Russel diagram (HRD) and the evolution of the rotation velocity of the secondary of this system when the accreted material is assigned different values of specific angular momentum. In all systems with $M_1 = 1.25\ M_\odot$ the mass transfer is assumed to start at $t = 3.06$ Gyr. This point is identified by the circle numbered "1" in the figure. The $M_{2,\mathrm{i}} = 0.75\ M_\odot$ secondary at this age is still early on in its main sequence with a central hydrogen mass fraction of $X_{\mathrm{H,c}} = 0.59$ (down from the ZAMS value of 0.758). Once mass transfer starts, the tracks corresponding to different values of j_a separate.

The accretion rate of $\dot{M} = 10^{-6}\ M_\odot\,\mathrm{yr}^{-1}$ is high enough that the accretion timescale $\tau \simeq M_2/\dot{M}$ is always much shorter (by a factor of ten or more) than the thermal timescale of any CEMP star progenitor. Accreting material (part of the track between "1" and "2" in Fig. 1a) at this rate therefore drives the star out of thermal equilibrium to higher luminosity and effective temperature. Once accretion ends ("2"), the star attempts to return to equilibrium, becoming fainter and cooler in the process.

While returning to thermal equilibrium, the stars spin up for a time, both in absolute terms and as a fraction of the critical velocity (Figs. 1b,c). For the highest values of specific angular momentum the stars may reach critical rotation at some point, as in the $j_\mathrm{a} = 7 \times 10^{17}\ \mathrm{cm^2\,s^{-1}}$ case in this system (yellow line). Since our primary interest is the long-term evolution after relaxation, we do not attempt to model this brief ($\delta t \simeq \tau_{\mathrm{KH}}$) phase accurately, assuming that it is not very important for the subsequent evolution[2]. Instead, we simply limit the centrifugal acceleration, and the resulting structural deformation, while the star is formally rotating at super-critical velocities (dashed portion of the line). After relaxation, this particular model never exceeds $\Omega/\Omega_\mathrm{c} \simeq 0.8$.

Various aspects of the evolution of the star after it settles back on the main sequence ("3") depend on the angular momentum accreted. First, owing to the extra support against gravity from the centrifugal force, rotating stars are normally cooler and less luminous than non-rotating stars – they resemble non-rotating stars of lower mass (Sackmann 1970). Here this effect is largely compensated for by the unusual chemical structure. The non-rotating model is fairly cool ($T_\mathrm{eff} \simeq 6550$ K at turn-off, same as the $j_\mathrm{a} = 10^{15}\ \mathrm{cm^2\,s^{-1}}$ track and about 200 K less than a regular 0.8 $M_\odot$ star at $Z = 10^{-4}$) because of the high metallicity of the accreted material. Making the star rotate leads to dilution of this material by rotational mixing (Fig. 2), and the corresponding change in the opacity actually makes the star hotter (although not more luminous) at turn-off ("4") than in the non-rotating case[3]. Only for very rapid rotation rates ($\Omega/\Omega_\mathrm{c} \gtrsim 0.5$ or $v_\mathrm{rot} > 100\ \mathrm{km\,s^{-1}}$), when rotational mixing does not lead to significant further changes in the structure of the star, do the mechanical effects shift the track back to cooler temperatures. The resulting spread in turn-off temperatures between all models of this system is only about 100 K.

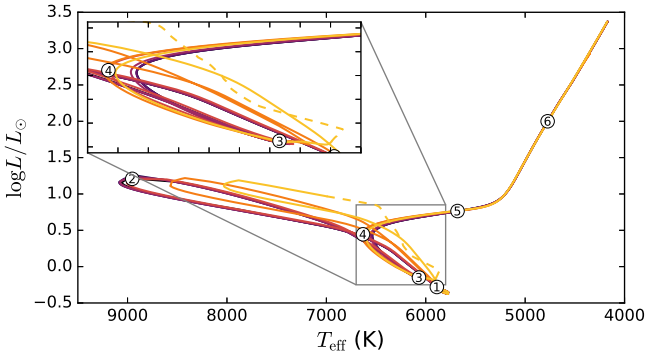

(a) Hertzsprung-Russell diagram

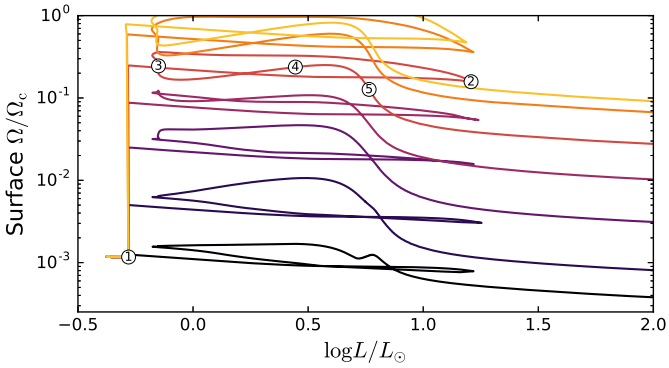

(b) Evolution of surface angular rotation velocity

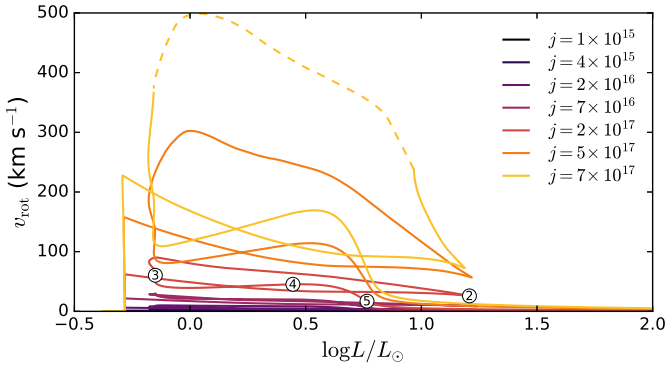

(c) Evolution of surface rotation velocity

Fig. 1. Evolution of a $M_{2,\mathrm{i}} = 0.75\ M_\odot$ secondary accreting $\Delta M = 0.05\ M_\odot$ of material from a primary with initial mass $M_1 = 1.25\ M_\odot$. Tracks distinguish different specific angular momentum of the accreted material. The numbers on top of the $j_\mathrm{a} = 2 \times 10^{17}\ \mathrm{cm^2\,s^{-1}}$ track mark the beginning of mass transfer (1), end of mass transfer (2), return to the main sequence (3), main sequence turn-off (4), beginning of first dredge-up (5), end of first dredge-up (6). The dashed part of the $j_\mathrm{a} = 7 \times 10^{17}\ \mathrm{cm^2\,s^{-1}}$ track marks the phase of the evolution where the star is formally above critical rotation (see text).

Second, the internal transport of angular momentum leads to different initial rotational evolution for rapid rotators. Normally, the surface value of Ω/Ω_c somewhat increases during the main sequence evolution of low-mass stars. This is a consequence of their slight expansion, which reduces the critical rotation velocity ($\Omega_\mathrm{c} \propto R^{-3/2}$). Here, in the rapid rotators, Ω/Ω_c and v_rot first decrease because the accreted momentum is transported inwards. After reaching a minimum, Ω/Ω_c then increases for the

[2] Presumably the star must shed the super-critical layers as it contracts. Unless the material is re-accreted later, the star then ends up with a slightly lower mass. In this particular case, losing about 0.004 $M_\odot$ of material during the contraction suffices to keep the star below critical rotation. This amount of mass loss has only a small effect on the subsequent evolution.

[3] To elaborate, models with rotation are indeed slightly cooler and less luminous early on in the post-mass-transfer main sequence. But by the time they reach turn-off, most of them are hotter as a result of the mixing.

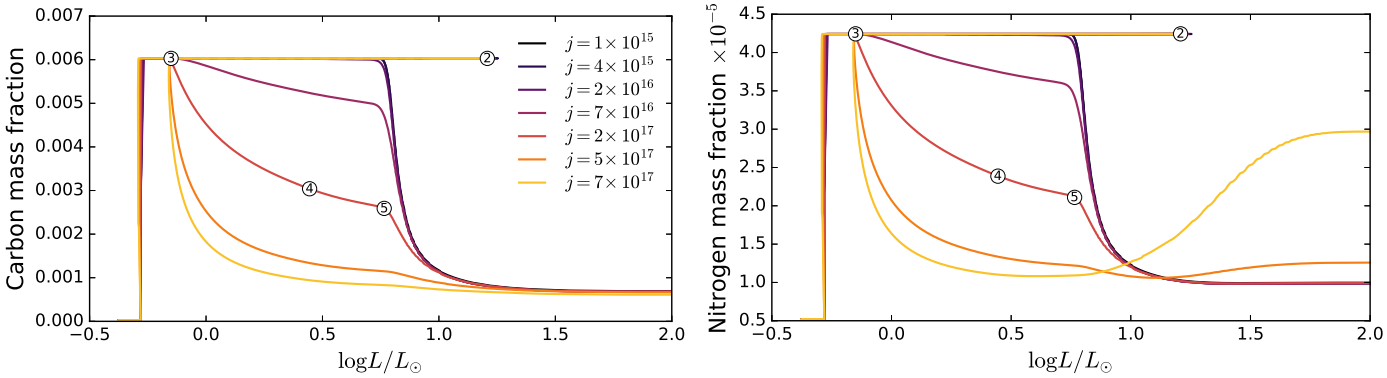

(a) Evolution of carbon

(b) Evolution of nitrogen

Fig. 2. As Fig. 1 but showing the evolution of the carbon and nitrogen surface mass fractions.

rest of the main sequence. All models reach a maximum in the rotation rate somewhere between the turn-off ("4") and the beginning of first dredge-up (FDU; "5").

Figure 3 shows the internal evolution of the rotational velocity profile in the star between the beginning of mass transfer and the end of FDU, and Fig. 4 shows the internal profiles of the specific angular momentum, angular rotation velocity, and carbon and nitrogen abundances near the main sequence turn-off for the different values of j_a. Naturally, accreting more angular momentum leads to deeper and faster transport of angular momentum. By the time the star reaches the turn-off in the $j_a = 7 \times 10^{16}$ cm^2 s^{-1} ($v_{rot} \simeq 20$ km s^{-1}) case, the angular momentum is mixed to about the half-way point in the star by mass. For the highest values of j_a ($v_{rot} \gtrsim 100$ km s^{-1}) nearly all of the star is mixed by then.

The mixing of angular momentum and of chemical elements does not occur to the same depth (cf. Figs. 4a and c). For example, in the lowest angular momentum case that shows a change in the surface abundances on the main sequence, $j_a = 7 \times 10^{16}$ cm^2 s^{-1} (Fig. 2), the chemical elements have been partially mixed down to a mass coordinate of $m \simeq 0.6\ M_\odot$ by the time the star has reached the turn-off. Meanwhile, the angular momentum has been transported about twice as deep. This is a direct consequence of the choice of f_c, the fraction of total angular momentum diffusion coefficient applied to chemical transport, in Eq. (4). Had we chosen $f_c = 1$, the depth of chemical and angular momentum transport would coincide. Instead, the timescale for chemical transport is much longer than that for angular momentum transport, and thus angular momentum has been transported to a greater depth at a given time. We return to the influence of f_c and f_μ in Sect. 4.3.

Which of the different processes dominates the transport of angular momentum? The answer changes over time (Fig. 5). At first, a steep Ω-gradient is present at the interface between the accreted layer and the original surface of the star. This induces shear mixing, which dominates the initial transport with some contribution from the GSF instability. But the transport also smears out the Ω-gradient, quenching the shear instability. For a while, the GSF instability is responsible for the continuing inward transport of angular momentum, until eventually much of the Ω-gradient is removed, and mixing proceeds over longer timescales by the Eddington-Sweet circulation (which is the only term in Eq. (2) that depends on Ω and not its gradient). Some Ω-gradients always remain (e.g. Fig. 3), but these are either too small to contribute to further mixing and/or the mixing is inhibited by molecular weight gradients. Given the rapid removal of the Ω-gradients, Eddington-Sweet circulation is responsible for most of the chemical mixing.

Once first dredge-up starts ("5"), the tracks again converge, and the evolution up the red giant branch (RGB) is similar in all cases. This is largely the result of FDU erasing most of the differences in the chemical structure between the model sequences. Furthermore, the accreted angular momentum is insufficient to result in large rotation rates (with respect to the critical rate) of any part of a giant because of its much larger moment of inertia.

Overall, below $j_a \lesssim 2 \times 10^{16}$ cm^2 s^{-1} (turn-off velocity of about 10 km s^{-1}) the evolution of the CEMP star in this system is essentially unaffected by the rotation. This is because both the centrifugal acceleration is too small to substantially lower the effective gravity, and the contrast between the accreted layer and the region below is too small to trigger significant chemical mixing of the two (although there is some angular momentum mixing; Fig. 4a). For higher values of j_a the timescale for chemical transport is finally short enough, compared to the nuclear timescale, that chemical dilution of the accreted material can occur before FDU (Fig. 2), which, as explained above, also shifts the track in the HRD. Naturally, the greater j_a, the more extensive and rapid the mixing. For the highest values of j_a mixing is deep enough that FDU no longer plays a significant role in diluting the accreted material. However, if rotational mixing on the main sequence is extensive enough to bring the accreted carbon down to regions where it can be burnt, FDU can bring the produced nitrogen, visible in Fig. 4d around $m \simeq 0.3\ M_\odot$, to the surface. In the two most rapidly rotating models, the nitrogen abundance after FDU ("6") is thus higher than in all others (Fig. 2b).

The evolution further up the giant branch is not very eventful in these models. No further abundance changes occur once FDU is over. The contracting core spins up and the expanding envelope slows down – the surface velocities decrease to $v_{rot} \lesssim 10$ km s^{-1}. There thus develops a large and ever-increasing contrast between the rotation rate of the core and the envelope (Fig. 3). This is not consistent with asteroseismic measurements of red giant core rotation rates (Mosser et al. 2012; Deheuvels et al. 2014), which find much greater coupling between the core and the envelope. This coupling is thought to come about as a result of magnetic fields (Spruit 2002; Suijs et al. 2008) and/or gravity waves (Talon & Charbonnel 2003, 2008; Fuller et al. 2014), neither of which we have modelled at this time. In terms of surface abundances, these processes seem more likely to manifest

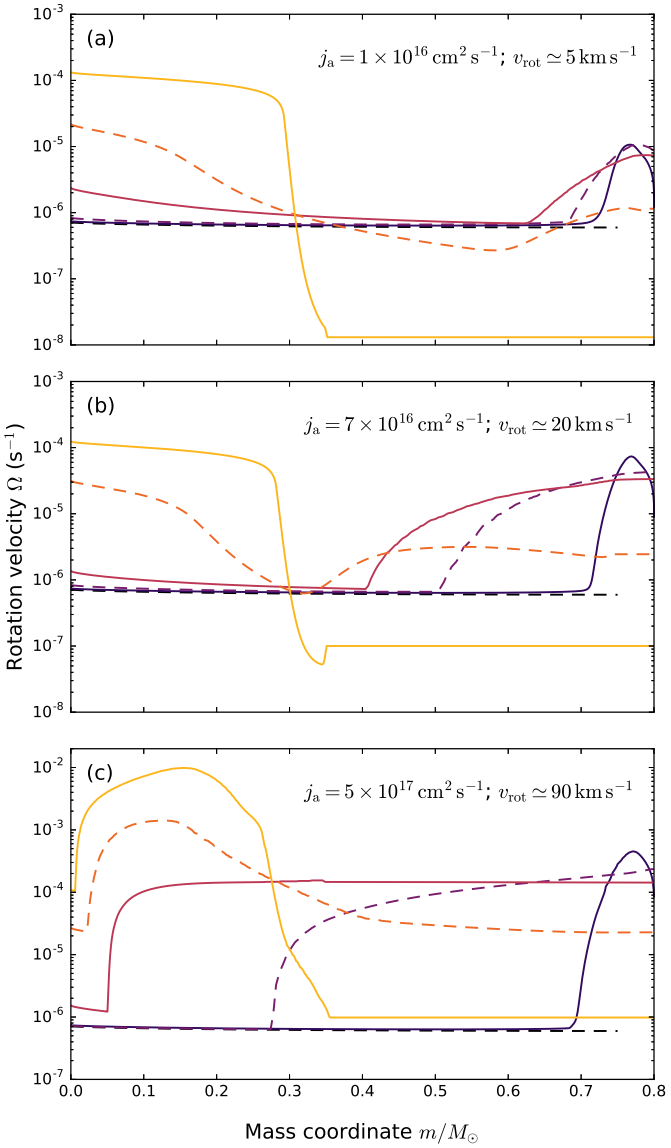

Fig. 3. Evolution of angular rotation velocity profiles for three different values of j_a. The dashed black profile corresponds to just before mass transfer ("1") and subsequent profiles, plotted in alternating line types of progressively lighter colours, correspond to end of mass transfer ("2"), return to thermal equilibrium ("3"), main sequence (between "3" and "4"), before first dredge-up ("5") and after first dredge-up ("6"). The last two profiles demonstrate the spin-up of the core after the main sequence. Note the different y scales.

by altering the importance of rotational mixing than leading to mixing directly (Talon & Charbonnel 2005; Maeder & Meynet 2005; Eggenberger et al. 2010), an effect that to some extent we probe by considering different rotation rates.

3.2. Models with atomic diffusion and thermohaline mixing

Atomic diffusion will tend to modify the surface abundances following mass transfer. In Matrozis & Stancliffe (2016) we showed how, in absence of other mixing processes, in most CEMP-*s* stars the carbon should settle out of the surface convection zone, while the surface abundance of iron should increase as a result of radiative levitation. Near the main sequence turn-off, before the convective envelope begins to move inwards in mass, the resulting abundances (e.g. [C/H] < -1 and [Fe/H] > -1 so that [C/Fe] < 0) can be very different from those of the accreted material ([C/H] $\simeq 0$ and [Fe/H] $\simeq -2$ so that [C/Fe] $\gtrsim 2$).

However, atomic diffusion will be counteracted by rotational mixing. As a result of this competition, abundance variations on the main sequence are expected in models of all rotation rates (Fig. 6a). At the lowest rotation velocities atomic diffusion dominates, modifying the surface abundances of metals until the convective envelope mass begins to increase shortly after the turn-off. But even a model rotating at less than a kilometer per second shows a slightly reduced effect compared to the non-rotating case. As one considers higher rotation rates, atomic diffusion near the surface is more and more inhibited up to the $j_a = 2 \times 10^{16}$ cm^2 s^{-1} case (in this system corresponding to a turn-off velocity of $v_{rot} \simeq 9$ km s^{-1}), where the abundance variations are smallest, and the surface abundances remain within 15% of the accreted composition. In non-diffusing models this is the highest j_a case in which there is practically no change in the abundances prior to first dredge-up (Fig. 2). As j_a is increased still further, rotational mixing takes over, and the models look more and more like in the purely rotating case in terms of surface abundances.

The competition between diffusion and rotational mixing also has an effect on the global properties of the star. It has been shown (e.g. VandenBerg et al. 2002; Bressan et al. 2012) that non-rotating models without atomic diffusion are longer-lived and hotter throughout the main sequence evolution than models with diffusion. This holds also for models of CEMP-*s* stars. But, because of partial inhibition of atomic diffusion, accreting even a small amount of angular momentum makes a model more like a non-diffusing one and thus hotter throughout the main sequence than a model with diffusion only (Fig. 6b). When the angular momentum accreted is sufficient to cause rotational mixing directly ($j_a \gtrsim 7 \times 10^{16}$ cm^2 s^{-1}), the models become still hotter. Since the surface abundance anomalies are actually smaller than in the non-rotating case, this must be due to inhibition of diffusion deeper in the star. Eventually, the mechanical effects from rotation take over such that the models with highest rotation rates are again cooler.

Thermohaline mixing, when modelled as an independent process (see Sect. 4.2), always dominates over diffusion and rotational mixing. In this system thermohaline mixing rapidly reduces the carbon abundance by a factor of about six (between $\log L \simeq 0.2$ and -0.1; Figs. 7a,b). Once thermohaline mixing has leveled the inverse μ-gradient, diffusion modifies the surface abundances still further in the slowly rotating models. In the rapidly rotating models the subsequent abundance evolution depends on the depth of thermohaline mixing. When this depth is at least comparable to that of rotational mixing (such as in this system, where thermohaline mixing proceeds down to a mass coordinate of $m \simeq 0.39\ M_\odot$), the chief role of rotational mixing is to inhibit atomic diffusion – it does not lead to significant further abundance changes before FDU. In systems where thermohaline mixing is not as deep (because of a smaller μ-gradient), rotational mixing can lead to further dilution of the accreted material.

A slight increase in the surface nitrogen abundance following FDU is found in this system even without rotation (Fig. 7b). This nitrogen has been produced from the accreted carbon transported deep into the star by thermohaline mixing (Stancliffe et al. 2007). Rotational mixing replenishes the carbon at these depths after thermohaline mixing has shut off so that more nitrogen can be produced, boosting the amount of nitrogen that is brought to the surface during FDU. Thermohaline

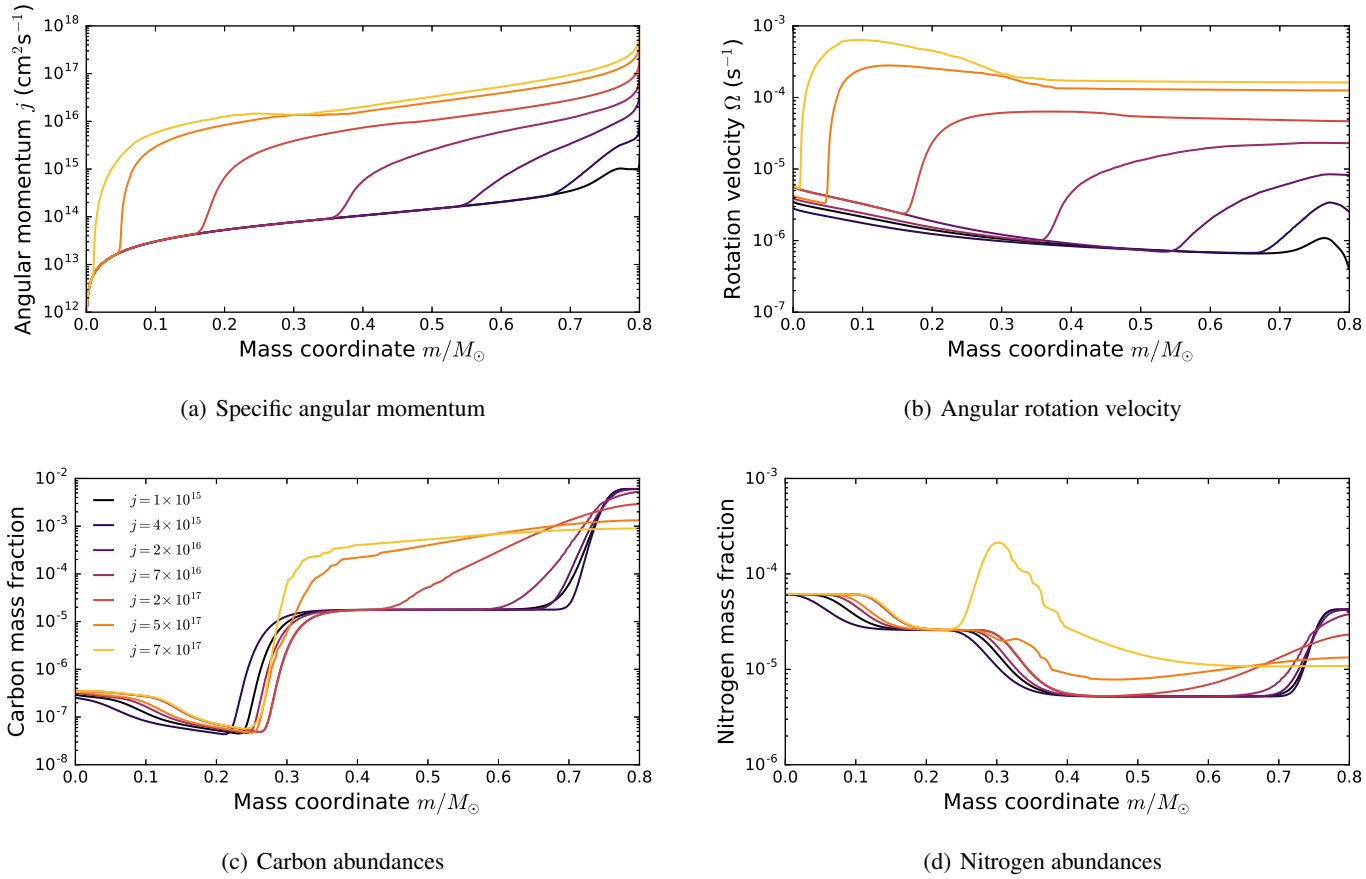

(a) Specific angular momentum

(b) Angular rotation velocity

(c) Carbon abundances

(d) Nitrogen abundances

Fig. 4. Distribution of various quantities near the end of the main sequence in the rotating models shown in Fig. 1.

mixing can once again activate following the RGB luminosity bump because of the ^{3}He(^{3}He, 2p)^{4}He reaction, which reduces the mean molecular weight just above the hydrogen burning shell (Eggleton et al. 2006; Stancliffe et al. 2009). A further increase in surface nitrogen abundance follows, but normally by no more than a factor of two because of the low value of the thermohaline mixing coefficient (Denissenkov 2010).

The mechanical effects are visible earlier and more clearly in models with thermohaline mixing, because most of the chemical mixing is caused by the thermohaline instability. Since this makes rotational mixing of chemical composition largely superfluous, only the mechanical effects from rotation remain. The spread in temperature around the main sequence turn-off is smaller than in models without thermohaline mixing (about 100 K versus 220 K, respectively; cf. Figs. 7c and 6b).

3.3. Abundance anomalies near the turn-off

We now attempt to characterize how the surface composition changes (from the composition of the accreted material) in all of our simulations collectively. We refer to these changes as abundance anomalies. In models where atomic diffusion dominates, the abundance anomalies are usually largest around the main sequence turn-off, which is thus a convenient point of reference for comparing different systems (Matrozis & Stancliffe 2016). In models without diffusion, or when diffusion is inhibited, the abundances of most elements instead change monotonically throughout the main sequence and beyond, as the accreted material gets more and more diluted (Fig. 2; this is not true for elements like nitrogen that can undergo further nuclear processing). Since a similar point of reference in these models thus cannot be identified, we adopt the same point, the main sequence turn-off, for convenience.

In the system discussed above, accretion of material with specific angular momentum $j_a \lesssim 2\times10^{16}$ cm^2 s^{-1} has little influence on the evolution following mass transfer, if atomic diffusion is ignored. Figure 8 shows that this is the case in other systems (with different values of $M_{2,i}$, ΔM, and $M_{2,f}$) as well. It is the specific angular momentum (instead of, e.g., the total angular momentum accreted) that is decisive in determining whether material will mix, because material with higher specific angular momentum establishes a greater gradient in the angular velocity, which aids the shear instability.

In the same system, accretion of material with specific angular momentum $j_a = 2\times10^{16}$ cm^2 s^{-1} results in a turn-off velocity of about 10 km s^{-1}. In systems with other combinations of $M_{2,f}$, ΔM and M_1 the turn-off velocity can be anywhere between $v_{rot} \simeq$ 1–30 km s^{-1} (increasing with ΔM), with the range of possible turn-off velocities increasing with j_a (Fig. 9). That is because the rotation velocity of the star following mass accretion reflects the total angular momentum accreted. It does not constrain the amount of mass accreted, because the same amount of angular momentum can be obtained by accreting a small amount of material with high specific angular momentum, or a large amount of material with low specific angular momentum.

The rotation velocity is therefore not very informative of the amount of rotational mixing expected, which is unfortunate given that the rotation velocity is an observable quantity. A rotation rate of, e.g. 50 km s^{-1} could correspond to a carbon dilution of more than a dex if ΔM is small ($\lesssim$0.01 $M_\odot$) or negligible dilution if ΔM is large ($\gtrsim$0.2 $M_\odot$; Fig. 10). The rotation velocity

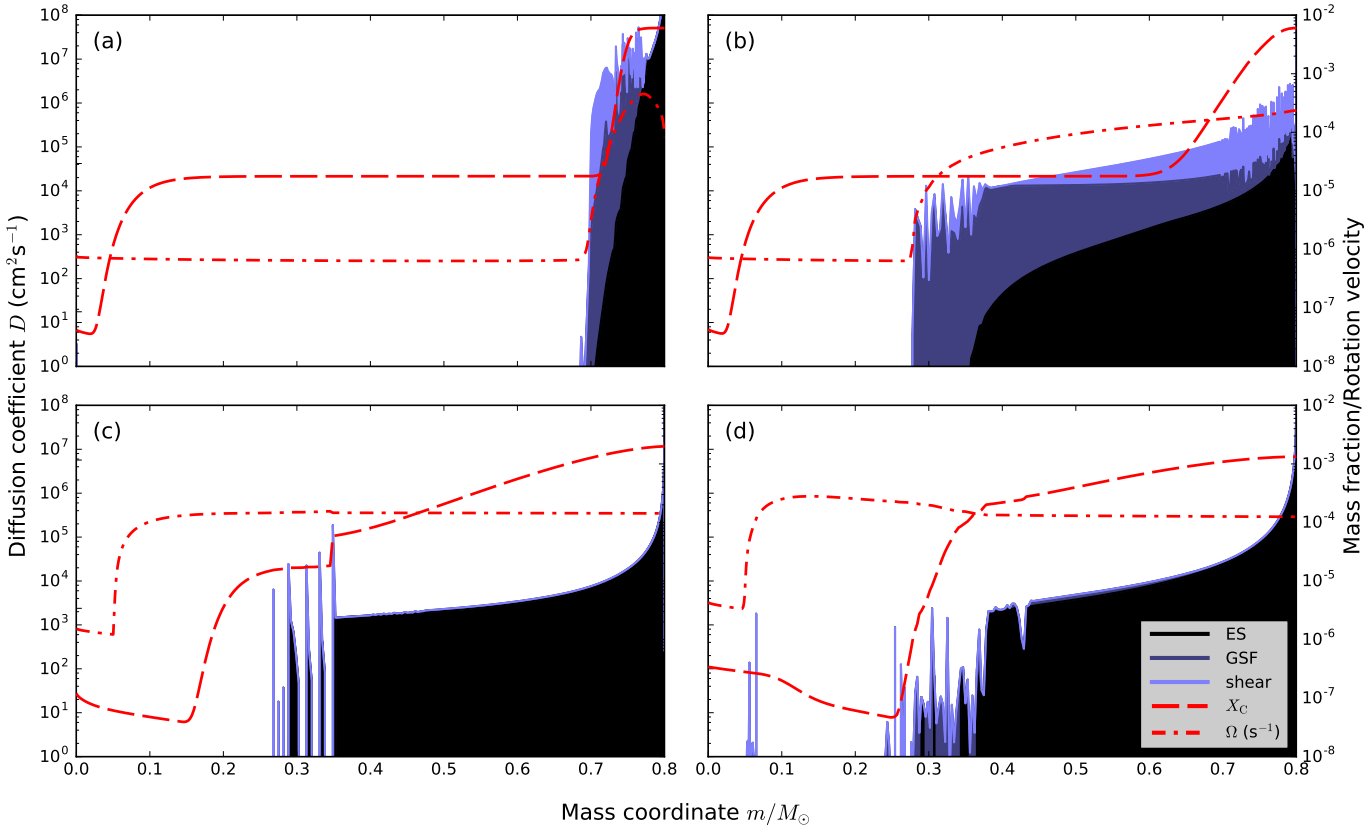

Fig. 5. Individual contributions of the most important rotational instabilities to the total angular momentum transport coefficient in the $j_a = 5 \times 10^{17}$ cm^2 s^{-1} ($v_{rot} \simeq 100$ km s^{-1}) case at four instances: *panel a*: shortly after mass transfer ends ("2"); *panel b*: near return to equilibrium ("3"); *panel c*: main sequence (between "3" and "4"); *panel d*: main sequence turn-off ("4"). Initially, large Ω-gradients favour the shear and GSF instabilities. Later on, when the Ω-gradients are erased, the overall transport is dominated by the Eddington-Sweet circulation. The lines show the angular velocity (dash-dotted) and the carbon abundance (dashed) profiles at the corresponding times.

does, however, serve as a good indicator of whether atomic diffusion should be important (Fig. 11). If one compares models with rotation alone (black symbols) to those with rotation and diffusion (orange symbols), one sees that only below $v_{rot} \simeq 1$ km s^{-1} does atomic diffusion lead to abundance anomalies of a dex or more. The amount of dilution of carbon drops below a factor of two above rotation velocities of a mere 2–3 km s^{-1} and basically disappears above 5 km s^{-1}. The most severe change in abundances in models with such rotation velocities results from thermohaline mixing (blue symbols), which typically reduces [C/H] by a factor of three or more, depending on the mass accreted and the molecular weight of the accreted material (Stancliffe et al. 2007; Matrozis & Stancliffe 2016).

For the largest values of specific angular momentum ($j_a \gtrsim 7 \times 10^{17}$ cm^2 s^{-1}) abundance differences between models with and without thermohaline mixing also disappear. This is because, when rotational mixing is rapid enough, it can dilute the material to a similar extent as thermohaline mixing, and the abundances near the turn-off end up being similar (cf. Figs. 2a and 7a). Nevertheless, thermohaline mixing is still by far the more rapid of the two mixing processes and responsible for most of the dilution when $\Delta M \gtrsim 0.01\ M_\odot$ (as in the high-j_a cases in Fig. 7).

Overall then, in models with rotational mixing only, it is the specific angular momentum of the accreted material, and not the rotation velocity or the total angular momentum accreted, that best predicts whether rotational instabilities will directly lead to chemical mixing. For a given progenitor system (combination of M_1, $M_{2,i}$), the dilution on the main sequence is determined almost entirely by the specific angular momentum of the accreted material if more than a couple of hundredths of a solar mass are accreted. The rotation velocity, while not a reliable indicator of the importance of rotational mixing, does reflect the importance of atomic diffusion – large abundance anomalies above rotation velocities of a few km s^{-1} are not expected. Thermohaline mixing is responsible for most of the abundance changes occurring on the main sequence after mass transfer, unless very little mass is accreted (of the order of $10^{-3}\ M_\odot$).

4. Discussion

Following up on our previous work, we have modelled the evolution of a large number of CEMP-*s* stars originating from a range of putative progenitor systems, for the first time considering in detail the accretion and internal transport of angular momentum by these stars. We now discuss the applicability of the models to real CEMP-*s* stars (Sect. 4.1) and then turn to the abundance evolution predicted by the models in context of observations (Sect. 4.2). We end with an examination of the importance of the free parameters inherent in our adopted prescription for angular momentum evolution (Sect. 4.3).

4.1. Angular momentum content of real CEMP-s stars

We know of no CEMP-*s* stars rotating at a substantial fraction of their critical velocity. Indeed, typical velocities of CEMP dwarfs seem to be in the 5–15 km s^{-1} range (Masseron et al. 2012). These velocities are probably higher than the typical velocities of

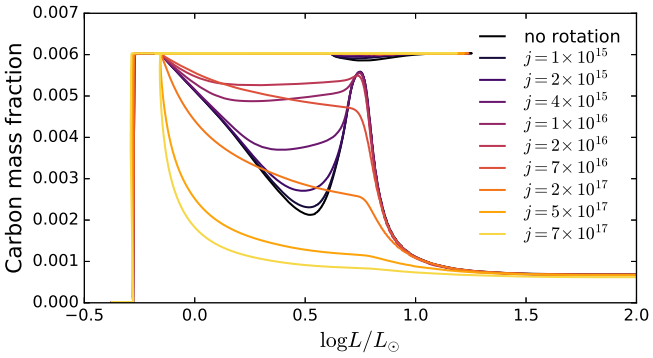

(a) Evolution of carbon

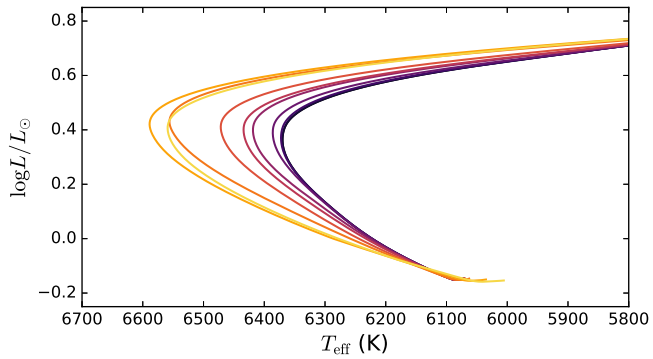

(b) Hertzsprung-Russell diagram

Fig. 6. Evolution and abundances of a $M_{2,\rm i} = 0.75\ M_\odot$ secondary accreting $\Delta M = 0.05\ M_\odot$ of material from a $M_1 = 1.25\ M_\odot$ primary for different values of specific angular momentum of accreted material (with atomic diffusion).

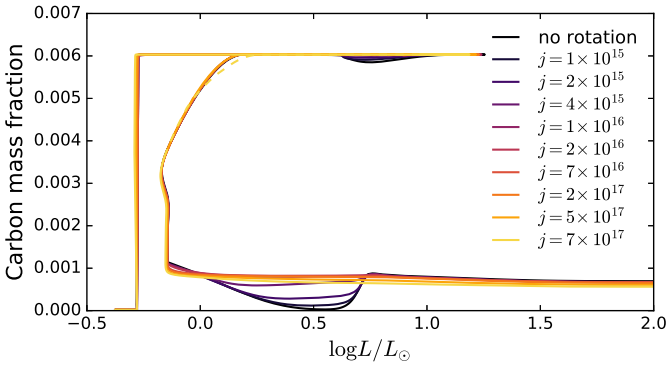

(a) Evolution of carbon

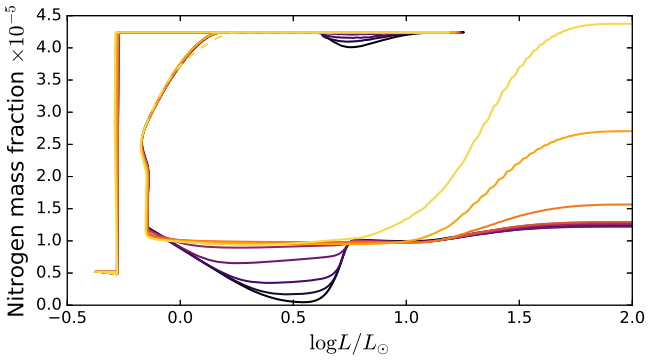

(b) Evolution of nitrogen

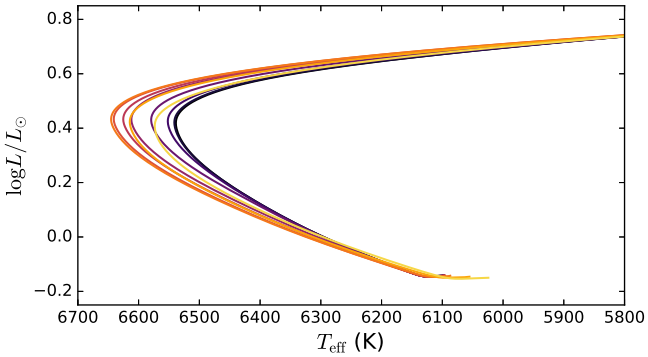

(c) Hertzsprung-Russell diagram

Fig. 7. As Fig. 6 but with thermohaline mixing.

old Halo dwarfs (by a factor of about two; Lucatello & Gratton 2003; Cortés et al. 2009), which supports the idea of angular momentum accretion by these stars. Even so, these velocities are quite low (no more than a few percent of the critical velocity), which indicates that either the stars lose angular momentum after mass transfer, or they accrete little of it to begin with. There are issues with both possibilities.

If a substantial amount of mass is to be accreted, accreting a small amount of angular momentum requires that the specific angular momentum of the accreted material is low, notably much below the Keplerian value of $j_{\rm K} = \sqrt{GMR} \simeq 2 \times 10^{18}$ cm^2 s^{-1} (Fig. 9). But multi-dimensional hydrodynamic simulations of representative progenitor systems routinely predict accretion disk formation (e.g. Theuns et al. 1996; Huarte-Espinosa et al. 2013; Chen et al. 2017) or otherwise find the specific angular momentum of the material flowing around the accretor to be close to $j_{\rm K}$ (Liu et al. 2017). Although these simulations neglect physical processes that likely play an important role in regulating the angular momentum accreted by the star (particularly magnetic fields; Armitage & Clarke 1996; Matt & Pudritz 2005a,b), the angular momentum would have to effectively be wrong by two orders of magnitude to reconcile the simulations with the observations. This issue is discussed in more detail in Matrozis et al. (2017).

Alternatively, the stars may have rotated rapidly shortly after mass transfer, but lost much of the accreted angular momentum subsequently. Given that their interior structure (a radiative interior with a surface convective envelope) is qualitatively similar to solar-like stars, one might expect that CEMP stars too lose angular momentum by magnetized winds (Weber & Davis 1967; Mestel & Spruit 1987). At solar metallicity this magnetic braking is found to cause the gradual spin-down of stars up to masses of $M \simeq 1.4\ M_\odot$ on timescales of about 0.1–1 Gyr (e.g. Skumanich 1972; Kawaler 1987; Meibom et al. 2011, 2015; Bouvier et al. 2014). If magnetic braking operates similarly in CEMP stars, they should have had a fair amount of time to spin down, as even the youngest CEMP stars are probably at least a gigayear old[4].

[4] The youngest Halo stars are about 10 Gyr old, while the lifetime of the lowest-mass star that undergoes third dredge-up during the AGB stage at $Z = 10^{-4}$ is about a gigayear less (Karakas 2010).

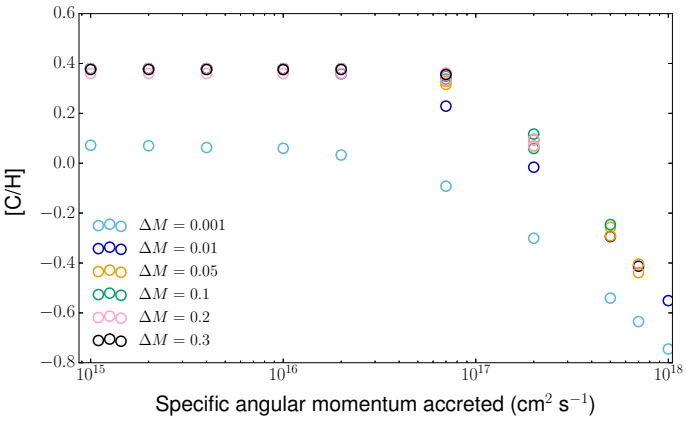

Fig. 8. Carbon abundance at main sequence turn-off as a function of specific angular momentum of accreted material in models with rotational mixing only. To avoid excessive crowding, only models with $M_1 = 1.25\ M_\odot$ are plotted, in which [C/H] $\simeq 0.38$ after mass transfer in all cases. The general result of little to no dilution for $j_a \lesssim 2\times10^{16}$ cm^2 s^{-1} holds for systems with other primary masses.

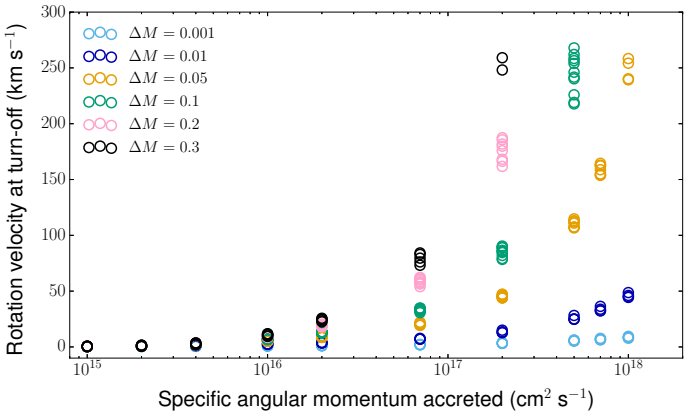

Fig. 9. Rotation velocities at main sequence turn-off ("4") resulting from accretion of material of different specific angular momentum in all simulations with rotational mixing only. The critical velocity at turn-off is between about 280 and 300 km s^{-1} in the vast majority of cases.

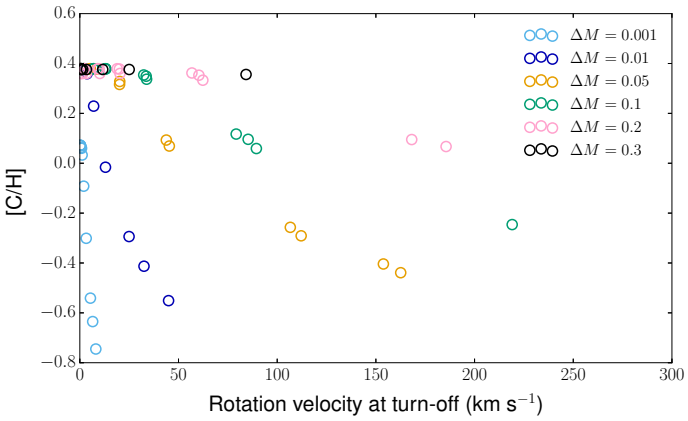

Fig. 10. Carbon abundance at turn-off ("4") as a function of rotation velocity in models with $M_1 = 1.25\ M_\odot$ and rotational mixing only. After mass transfer [C/H] $\simeq 0.38$ in all cases.

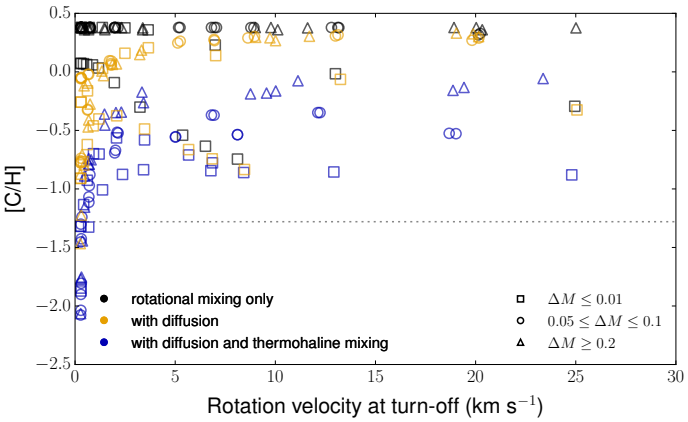

Fig. 11. Carbon abundance at turn-off ("4") as a function of rotation velocity in all models with $M_1 = 1.25\ M_\odot$. After mass transfer [C/H] $\simeq 0.38$ in all cases. Models above the dotted line are carbon-enhanced ([C/Fe] > 0.9; Masseron et al. 2010).

The magnetized winds are believed to be powered by a dynamo sustained by the interaction between differential rotation near the base of the envelope and convection (Brandenburg & Subramanian 2005; Charbonneau 2010). The successful operation of the dynamo thus depends on the properties of the surface convection zone. As a prerequisite, one has to exist, and the progressively longer spin-down timescales of stars in the $1.1 \lesssim M/M_\odot \lesssim 1.4$ range is attributed to the gradual thinning of the surface convection zone (Kraft 1967; Kawaler 1987), after the disappearance of which no braking occurs. We find that by various measures that could be relevant for the efficiency of the dynamo (e.g. Noyes et al. 1984; Schrijver 1993) – the mass contained ($10^{-5} \lesssim M_{\rm env}/M_\odot \lesssim 10^{-3}$), the convective turn-over timescale ($1 \lesssim \tau_{\rm conv}$(d) $\lesssim 10$), the fractional radius ($0.05 \lesssim R_{\rm env}/R \lesssim 0.2$) and volume ($0.15 \lesssim V_{\rm env}/V \lesssim 0.5$) – the convective envelopes of $Z = 10^{-4}$ models with $M \simeq 0.75$–$0.85\ M_\odot$ resemble those of $Z = 0.02$ models with $M \simeq 1.15$–$1.4\ M_\odot$ throughout much of the main sequence. The envelopes of CEMP stars are still more sizeable because of the increased metallicity (Z). It thus seems plausible that CEMP stars too could sustain a dynamo and undergo magnetic braking, although possibly on fairly long (gigayear) timescales.

Assuming CEMP stars do undergo magnetic braking, what are the consequences for their evolution? Obviously, one consequence is that their surface rotational velocity decreases over time, but what about the internal transport of angular momentum and chemical elements? To gain some insight into this question, we return to the illustrative case of Sect. 3.1 with $j_a = 5\times10^{17}$ cm^2 s^{-1}. We restart the model sequence from the end of mass transfer (labelled "2" in Fig. 1), this time including angular momentum loss following Kawaler (1988):

$$\frac{{\rm d}J}{{\rm d}t} = -K\left(\frac{R/R_\odot}{M/M_\odot}\right)^{\frac{1}{2}} \Omega \min(\Omega, \Omega_{\rm sat})^2. \quad (5)$$

$\Omega_{\rm sat}$ is the surface angular velocity, above which angular momentum loss is found to saturate in rapidly rotating solar-like stars (Chaboyer et al. 1995a), here taken to be $10\Omega_\odot$ (Amard et al. 2016), and $K = 2.5\times10^{47}$ (g cm^2 s) is a calibrating constant, chosen to reproduce the solar rotation rate at the solar age.

The default $M_{2,\rm f} = 0.8\ M_\odot$ model rotates at a velocity of $v_{\rm rot} \simeq 100$ km s^{-1} throughout the post-mass-transfer main sequence (Fig. 1c). Such rapid rotation implies a large torque according to Eq. (5). Its application to the relatively thin envelope ($0.004\ M_\odot$ shortly after mass transfer) of the star results

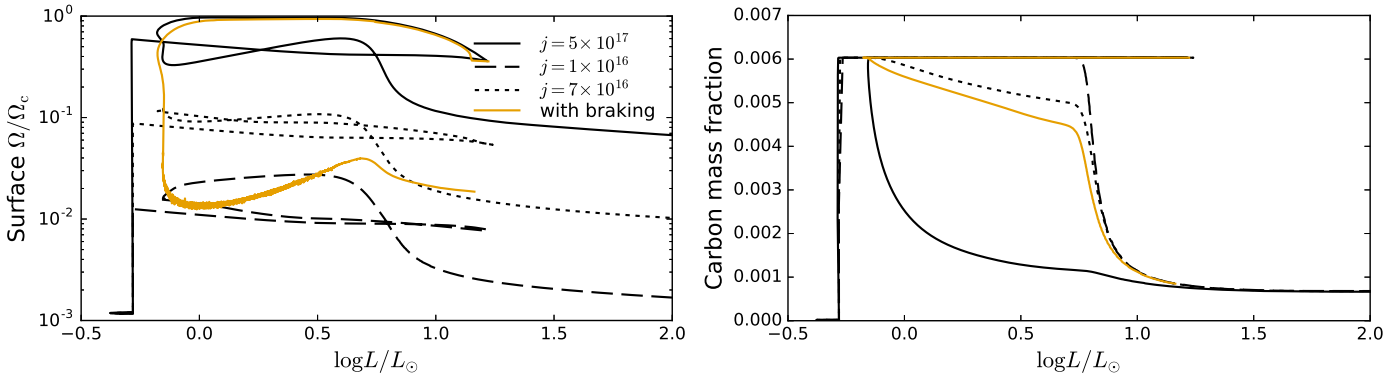

(a) Evolution of surface rotation velocity (b) Evolution of carbon

Fig. 12. Influence of magnetic braking on the $M_1 = 1.25\ M_\odot$, $M_{2,i} = 0.75\ M_\odot$, $\Delta M = 0.05\ M_\odot$ model with $j_a = 5 \times 10^{17}$ cm^2 s^{-1} and rotational mixing only. Out of the models without braking, on the main sequence the $j_a = 1 \times 10^{16}$ cm^2 s^{-1} model is the one most similar in terms of surface rotation velocity, and the $j_a = 7 \times 10^{16}$ cm^2 s^{-1} model is the one most similar in terms of surface abundances.

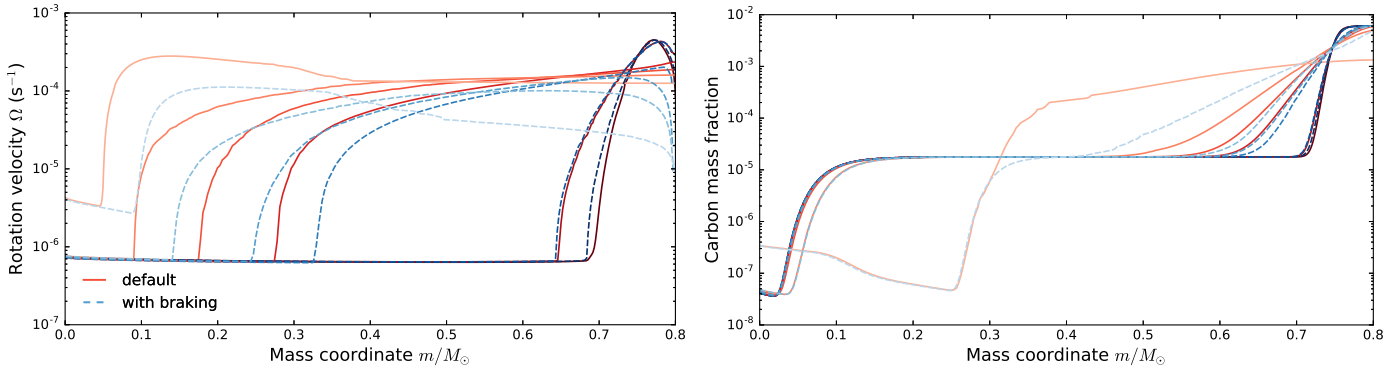

(a) Evolution of internal rotation profiles (b) Evolution of internal carbon profile

Fig. 13. Internal evolution of the model from Fig. 12 with and without magnetic braking. The sets of profiles correspond to very similar ages in both cases, and later times are plotted in progressively lighter shades.

in a very rapid spin-down: 50 Myr after the end of mass transfer the surface rotation velocity has fallen to $v_{rot} < 10$ km s^{-1} and after about a gigayear it levels off to $v_{rot} \simeq 4$ km s^{-1} (Fig. 12a). After that the angular momentum of the envelope no longer changes appreciably, as the angular momentum loss is balanced by the outward transport from the radiative core. In other words, the angular momentum is then extracted from the core (Pinsonneault et al. 1991; Epstein & Pinsonneault 2014).

The surface rotational velocity of the model with magnetic braking during the main sequence is most similar to that with $j_a = 10^{16}$ cm^2 s^{-1} and no braking. But the internal angular momentum evolution is not very different from the default model with $j_a = 5 \times 10^{17}$ cm^2 s^{-1} because the accreted layer is much larger than the convective envelope. The instabilities at the base of this accreted layer thus still occur, although the continuous removal of angular momentum does reduce the depth to which angular momentum has been transported at a given time (Fig. 13). Still, the angular momentum content in the model with braking remains larger than in the $j_a = 10^{16}$ cm^2 s^{-1} model without braking, and this is reflected by its more rapid rotation during post-main-sequence evolution.

Since the transport of chemical species occurs over a longer timescale, it is more affected by the angular momentum loss at the surface. The depth to which elements are mixed is much smaller in the case with braking ($m \simeq 0.45\ M_\odot$ instead of $m < 0.3\ M_\odot$ at turn-off; Fig. 13b), and the surface abundance evolution on the main sequence is closer to the $j_a = 7 \times 10^{16}$ cm^2 s^{-1} case, which has a surface rotational velocity of only $v_{rot} \simeq 20$ km s^{-1} (Fig. 12). Internally, however, the abundance profiles are very smeared out in the model with braking. This results in a prolonged first dredge-up, compared to the $j_a = 7 \times 10^{16}$ cm^2 s^{-1} case.

For this system then, including magnetic braking in the case with $j_a = 5 \times 10^{17}$ cm^2 s^{-1} gives a surface rotational velocity similar to the $j_a = 10^{16}$ cm^2 s^{-1} case, and surface abundance evolution similar to the $j_a = 7 \times 10^{16}$ cm^2 s^{-1} case. We expect that the former would remain true, if we had applied magnetic braking to a model with a different value of $j_a > 10^{16}$ cm^2 s^{-1}, or to some extent even a different system (i.e. combination of M_1, $M_{2,i}$, ΔM) altogether. The reason is that the surface velocity after the envelope has spun down largely depends on the constant K in Eq. (5). But the non-braking model with the most similar evolution of surface abundances would however change (to a case somewhere between that which gives the most similar rotation velocity, and that from which we start). But generally, we expect magnetic braking to reduce the surface abundance anomalies stemming from rotational mixing. For example, all the points in Fig. 10 would shift towards lower velocities and

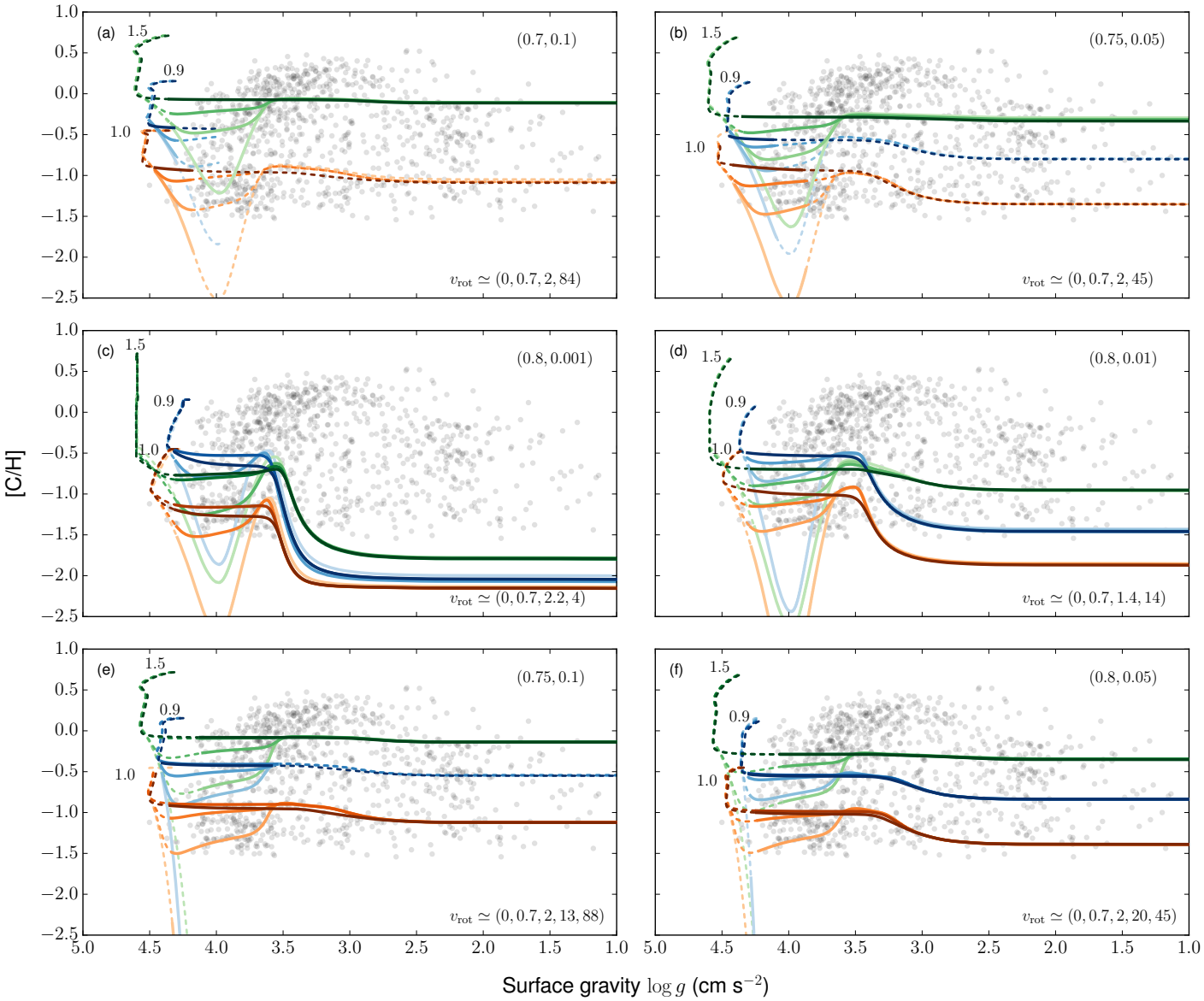

Fig. 14. Evolution of [C/H] in CEMP-*s* star models of different initial and accreted masses (given in solar masses in the top right corner of each panel) with rotational mixing, gravitational settling, and thermohaline mixing. The three sets of lines correspond to different AGB donor masses (marked on the left). The colour intensity indicates the specific angular momentum of accreted material. From brightest to darkest, the lines correspond to $j_{\rm a} = 0$ (no rotation), $0.02, 0.04, 0.2, 0.7, 2.0$ ($\times 10^{17}$ cm^2 s^{-1}). The corresponding rotation velocities are listed in the bottom right corner of each panel (to reduce crowding not all $j_{\rm a}$ cases are shown in every panel). The solid part of each line delimits ages between 10 and 13.8 Gyr (for panel a computations were stopped at $t = 16$ Gyr). The points are CEMP stars ([C/Fe] ≥ 0.9; Masseron et al. 2010) from SDSS with $-2.5 \leq$ [Fe/H] ≤ -2.0 (Lee et al. 2013).

to higher [C/H], the shift in velocity being more important for models with $\Delta M \gtrsim 0.05\ M_\odot$, and the shift in [C/H] dominating for models with $\Delta M \lesssim 0.01\ M_\odot$.

4.2. Comparison to observations

In Matrozis & Stancliffe (2016) we showed that atomic diffusion should lead to very large abundance anomalies (e.g. [C/Fe] < -1) near the main sequence turn-off, a result clearly at odds with observational data. Here we again juxtapose some of our model sequences to the measured carbon abundances ([C/H]) of CEMP stars from the Sloan Digital Sky Survey (SDSS; Lee et al. 2013), the largest homogeneous data set of carbon abundances in metal-poor stars. We restrict the comparison to models with $v_{\rm rot} \lesssim 100$ km s^{-1} at turn-off. While this limit considerably exceeds the highest observed velocities of CEMP stars, these rapidly rotating models serve to illustrate the effect of rotational mixing in systems other than the one discussed so far, and can be taken to mimic the surface chemical evolution of initially still more rapidly rotating models with magnetic braking.

We also restrict the comparison to models with atomic diffusion. We can easily see when diffusion, or more accurately gravitational settling and thermal diffusion, becomes important by considering the [C/H] abundance evolution in models with different rotation velocities. In all cases in Fig. 14 we see that the hallmark pattern of atomic diffusion – continuous decrease of heavy element abundances until the turn-off ($\log g \simeq 4$ in these stars) followed by a reversal as the convective envelope moves

inwards – is severely disrupted, compared to the non-rotating case, already at $v_{\rm rot} \simeq 0.7$ km s^{-1}. For $v_{\rm rot} \simeq 2$ km s^{-1} the variation of [C/H] over the main sequence is below 0.3 dex. This is what we already concluded in Sect. 3.3 (Fig. 11). Although in this study we have ignored radiative levitation, which can drastically alter the relative abundances of metals (e.g. the [C/Fe] ratio; Matrozis & Stancliffe 2016), levitation will only be important together with the other microscopic diffusion processes, that is, in the slowly rotating models ($v_{\rm rot} \lesssim 2$ km s^{-1}).

If rotational mixing is indeed responsible for inhibiting atomic diffusion in metal-poor stars, the lack of stars with [C/H] < -2.5 between $-2.5 <$ [Fe/H] < -2 seems to require that all stars rotate, even if very slowly ($v_{\rm rot} \gtrsim 0.5$ km s^{-1}). Otherwise we should observe some carbon-depleted stars around the main sequence turn-off. Whether there are stars that rotate still slower seems unclear. Spectroscopically such low velocities are difficult to disentangle from other line broadening mechanisms (Valenti & Fischer 2005), and photometric missions are currently restricted to rotation rates above about the same limit ($P_{\rm rot} \lesssim 100$ d; Affer et al. 2012; McQuillan et al. 2014).

Whether thermohaline mixing should activate in rotating stars is a matter of debate. Following Cantiello & Langer (2010) and Charbonnel & Lagarde (2010), we have treated the thermohaline and rotational instabilities independently, neglecting their possible interaction (although, they still influence each other by changing the structure of the stellar models). Thus modelled, thermohaline mixing results in a relatively immediate and substantial (Δ[C/H] > 0.3) reduction of [C/H] following mass transfer. Therefore, large quantities ($\Delta M > 0.2\ M_\odot$) of high molecular weight material are required to reproduce the largest observed carbon enhancements. Also, mixing proceeds to slightly greater depths in more rapidly rotating models. In models with $\Delta M \gtrsim 0.05\ M_\odot$ the depth of thermohaline mixing generally exceeds the maximum depth reached by the convective envelope at the end of first dredge-up. In these models there is thus little to no change in [C/H] during FDU (but [N/H] can increase substantially; see Stancliffe et al. 2007).

However, many authors (Denissenkov & Pinsonneault 2008a; Vauclair & Théado 2012; Maeder et al. 2013) have argued that the strong horizontal turbulence expected in rotating stars (Zahn 1992) should at least curtail thermohaline mixing, if not outright suppress it (also see Medrano et al. 2014). If so, it might be more appropriate to exclude thermohaline mixing. But it is worth noting that the μ-inversion on the red giant branch, on which much of the cited discussion is focused, is much smaller than established by accretion of material ($\Delta\mu/\mu \propto 10^{-4}$ versus $\Delta\mu/\mu \gtrsim 0.01$) and develops gradually as a result of ^{3}He-burning instead of instantaneously, so complete suppression of thermohaline mixing seems less likely in CEMP-*s* stars. Given this theoretical uncertainty, in Fig. 15 we also show models without thermohaline mixing.

At rotation velocities typical of CEMP stars ($v_{\rm rot} \simeq$ 5–10 km s^{-1}) these models look very similar to previously published models with only convective mixing (Stancliffe et al. 2007; Stancliffe & Glebbeek 2008). That is, no significant changes in surface abundances occur in these models before FDU dilutes the accreted material. Before that point, rotational mixing prevents atomic diffusion but does not cause any significant dilution of the accreted material by itself (unless very little mass is accreted as in Figs. 15c and d). Based on the SDSS data, it is difficult to ascertain whether models with or without thermohaline mixing ought to be preferred. Some dilution of the accreted material around FDU may be required (e.g. few stars have [C/H] $\gtrsim 0$ beyond $\log g \simeq 3$; see also Denissenkov & Pinsonneault 2008b), but without any thermohaline mixing the dilution is too large unless ΔM commonly exceeds 0.2 $M_\odot$.

There is a conspicuous lack of unevolved ($\log g \gtrsim 4.2$) CEMP stars in the SDSS data, particularly ones with [C/Fe] $\gtrsim$ 1.5. As discussed in detail in Matrozis & Stancliffe (2016), this dearth cannot be explained as an effect of (inhibited) atomic diffusion. Unsurprisingly then, the new models with rotational mixing also predict the existence of stars with $\log g \gtrsim 4.2$ and [C/Fe] > 1. In particular, lower-mass CEMP-*s* stars ($M_{2,\rm f} \lesssim 0.8\ M_\odot$) and most CEMP-*s* stars with low-mass AGB companions ($M_1 \lesssim 1\ M_\odot$) should populate this region, assuming the ages of these stars are between 10 and 13.8 Gyr (solid sections of the lines in Figs. 14 and 15). Since a similar scarcity of CEMP dwarfs is not evident from high-resolution studies (e.g. as compiled in the SAGA database; Suda et al. 2008, 2011, 2017), we do not believe the issue rests with the models.

4.3. Influence of rotational mixing parameters

The diffusion coefficients in Eq. (2) have been derived making use of order-of-magnitude estimates of some of the length- and timescales involved, and are thus rather uncertain. The rotational mixing parameters, $f_{\rm c}$ and f_μ, have been introduced to somewhat correct for this (Pinsonneault et al. 1989; Heger et al. 2000). These efficiency parameters are typically calibrated against observed surface chemical enrichment of rapidly rotating massive stars (e.g. Yoon et al. 2006; Brott et al. 2011) or the destruction of fragile elements in the Sun and other stars (Pinsonneault et al. 1989; Chaboyer et al. 1995b; Fliegner et al. 1996; Venn et al. 2002), and our default values (Heger et al. 2000) fall in their typical ranges: $0.01 \lesssim f_{\rm c} \lesssim 0.1$ and $0 \lesssim f_\mu \lesssim 0.2$.

In effect, $f_{\rm c}$ simply sets the timescale for the chemical transport compared to angular momentum transport. Therefore, increasing $f_{\rm c}$ increases the rate and extent of chemical mixing. But the influence of f_μ, which sets the sensitivity of the rotational instabilities to molecular weight gradients, is more subtle. Since the various instabilities depend on μ-gradients in different ways, changing f_μ alters their relative importance in different regions of the star and over time. Normally stars build up positive molecular weight gradients in their interiors as they evolve, i.e. $\nabla_\mu > 0$. Accretion of AGB ejecta instead forms a negative ∇_μ in the transition region between the original and accreted material. In that region shear instabilities are more likely to set in as a result, independently of f_μ[5]. But in the central regions, where $\nabla_\mu > 0$, increasing f_μ stabilizes the medium against shear. For the ES circulation and the GSF instability μ-gradients are always considered inhibiting, so only the absolute value of ∇_μ matters. Reducing f_μ thus always helps these transport processes, while increasing f_μ suppresses them. Overall then, increasing f_μ will reduce the extent of both angular momentum and chemical transport.

To glean the importance of the rotational mixing parameters in our CEMP star models, we have experimented with changing one of them at a time. For $f_\mu = 0.05$ we have run additional models with $f_{\rm c} = 0.01$ or $f_{\rm c} = 0.1$, and for $f_{\rm c} = 1/30$ models with $f_\mu = 0$ or $f_\mu = 1$.

Figure 16 shows the effect $f_{\rm c}$ and f_μ have on the internal evolution of a CEMP star model characterized by $M_1 = 1.25\ M_\odot$, $M_{2,\rm i} = 0.8\ M_\odot$, $\Delta M = 0.05\ M_\odot$, and $j_{\rm a} = 5 \times 10^{17}$ cm^2 s^{-1}. As

[5] Strictly, increasing f_μ when $\nabla_\mu < 0$ does make the dynamical shear instability more likely, whereas the secular shear instability is favoured for any $\nabla_\mu < 0$ (regardless of f_μ). However, we find the secular instability to set in far more often.

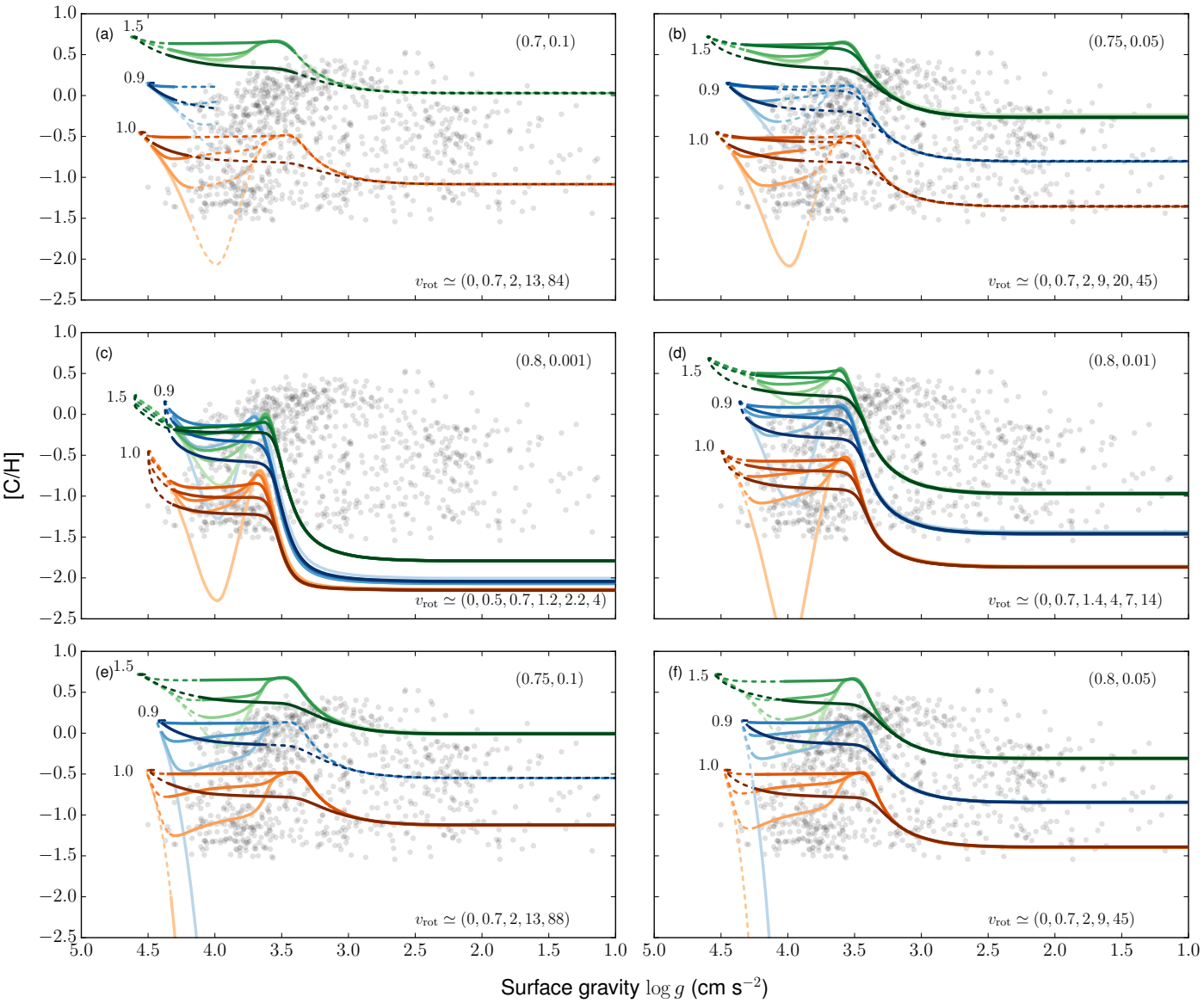

Fig. 15. As Fig. 14 but without thermohaline mixing.

expected, while f_c has almost no effect on the angular momentum evolution within the star (Fig. 16a), the extent and rate of chemical mixing correlates with f_c (Fig. 16b). Meanwhile, variation of f_μ affects the transport of both angular momentum and material. At $f_\mu = 1$ the transport of both is reduced, and by the end of the main sequence less of the star is mixed than in the default case.

The case with $f_\mu = 0$ is theoretically the most interesting one. Since the μ-gradients do not interfere with the transport, the extent of mixing depends primarily on its timescale. When it is sufficiently short compared to the evolutionary timescale, as is the case here, the angular momentum can be transported all the way to the centre of the star. In this particular case, starting from about a gigayear after mass transfer, the central regions rotate about a factor of a hundred faster than in the default model. This allows mixing of additional hydrogen into the burning regions and extends the main sequence lifetime by about 0.7 Gyr. Not only are such models longer lived (Fig. 17a), they also evolve considerably hotter because of their larger helium content, reaching much higher surface temperatures at turn-off ($T_{\rm eff} > 7000$ K; Fig. 17b). Such temperatures are not measured in CEMP stars, so rotational mixing in these stars cannot be efficient enough to cause substantial chemical mixing of the central regions. Observations would thus seem to rule out models with $f_\mu = 0$, but perhaps CEMP stars never acquire enough angular momentum, or lose it too rapidly, to allow for extensive rotational mixing in the first place (Sect. 4.1).

The internal evolution is naturally reflected by the surface abundances, as Figs. 17c,d demonstrate. In terms of surface abundances there is thus somewhat of a degeneracy between the specific angular momentum assigned to the accreted material and f_c (and f_μ to a lesser extent). For example, models with $f_c = 0.1$ resemble models with $f_c = 1/30$ and higher j_a. While this ambiguity is difficult to disentangle on a case-by-case basis, it does not influence some of the broader conclusions reached in previous sections. For example, in models with diffusion substantial abundance anomalies are still expected only at rotational velocities $v_{\rm rot} \lesssim 2$ km s^{-1} even in the two unfavourable cases with $f_c = 0.01$ and $f_\mu = 1.0$ (cf. Figs. 11 and 18).

Thus there are no strong constraints on f_c in the range [0.01, 0.1]. Outside of this range we expect that at least from the lower end f_c could be constrained (assuming that rotational mixing is

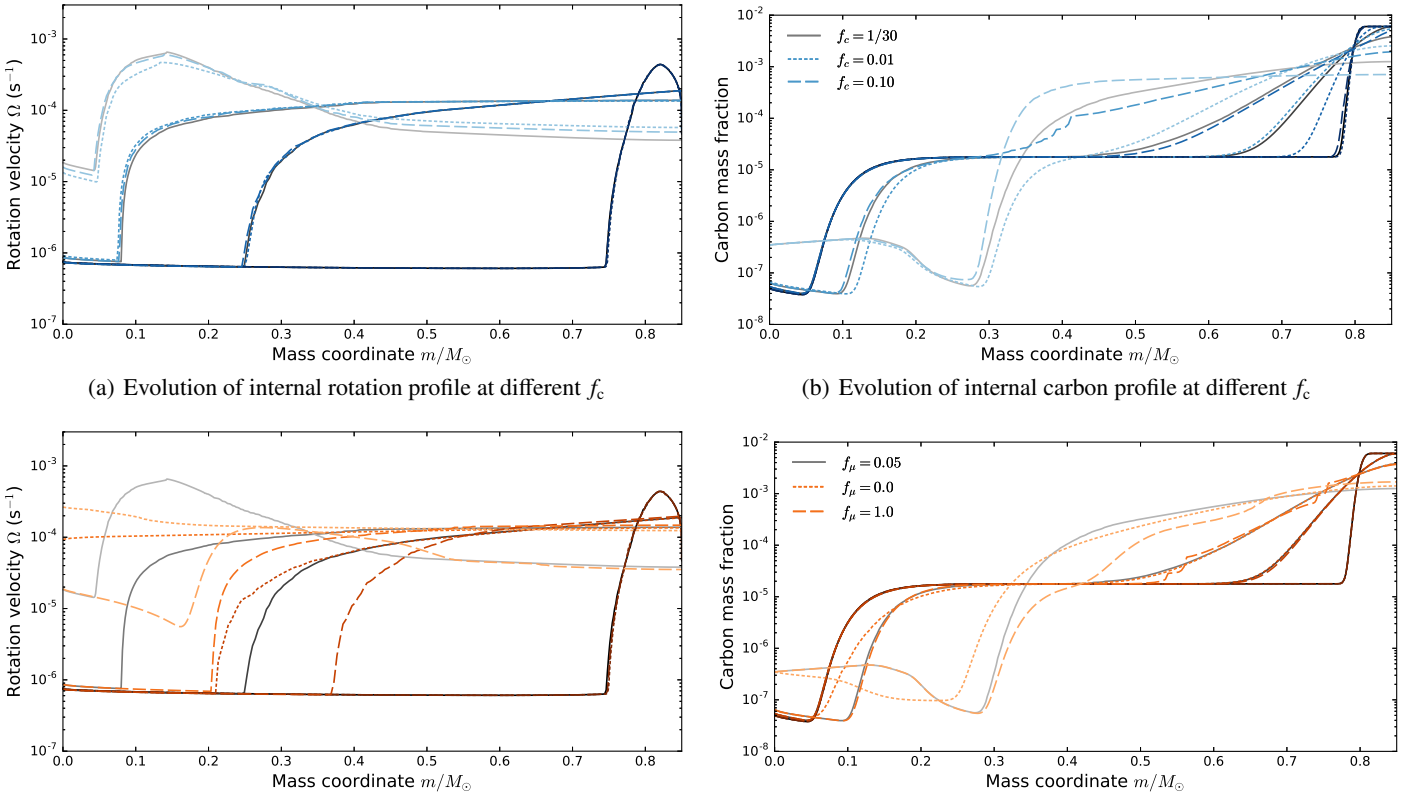

(a) Evolution of internal rotation profile at different f_c

(b) Evolution of internal carbon profile at different f_c

(c) Evolution of internal rotation profile at different f_μ

(d) Evolution of internal carbon profile at different f_μ

Fig. 16. Internal profiles for different rotational mixing parameters f_c (*panels a, b*) and f_μ (*c, d*) in the system with $M_1 = 1.25\ M_\odot$, $M_{2,i} = 0.8\ M_\odot$, $\Delta M = 0.05\ M_\odot$, $j_a = 5 \times 10^{17}$ cm^2 s^{-1}. The sets of profiles correspond to ages of about 3.06005 (darkest), 3.1, 4.5, and 11 Gyr (brightest) in all cases. Models with rotational mixing only.

indeed responsible for suppressing atomic diffusion). Eventually, for $f_c \ll 0.01$, the chemical transport due to rotational instabilities must become so slow that atomic diffusion would be expected to dominate the surface abundance evolution of CEMP stars, at odds with observations. Overall, because of the many steps involved in creating CEMP-*s* stars (nucleosynthesis in the AGB donor, mass and angular momentum accretion, and subsequent mixing of the accreted material), they could offer only loose constraints on f_c (and f_μ), which would in any case be consistent with more stringent constraints from other types of stars.

5. Summary and conclusions

We present a large number of models of *s*-process-rich carbon-enhanced metal-poor (CEMP-*s*) stars under the standard paradigm of mass accretion from an asymptotic giant branch donor. As a follow-up to Matrozis & Stancliffe (2016), for the first time we investigate what effect angular momentum accretion has on the chemical evolution of CEMP-*s* stars. The angular momentum deposited in the outer layers of the stars triggers rotational instabilities that induce mixing of angular momentum and the stellar material. We model the combined action of this rotational mixing with atomic diffusion (gravitational settling), and thermohaline mixing.

We can broadly summarize the relevance each of these processes has to different CEMP-*s* stars as follows. In the slowest rotating ($v_{\rm rot} \lesssim 1$ km s^{-1}) massive ($M_{2,f} \gtrsim 0.85\ M_\odot$) stars the greatest abundance changes are caused by atomic diffusion near the main sequence turn-off ($\log L \simeq 0.5$; $\log g \simeq 4$). Depending on the amount of mass accreted (and also the mean molecular weight of the accreted material), either first dredge-up (occurring during $3.5 \gtrsim \log g \gtrsim 3$) or thermohaline mixing ($\log g \simeq 4.5$) is more important in stars with moderate rotation velocities ($v_{\rm rot} \lesssim 20$ km s^{-1}), and also less massive CEMP-*s* stars ($M_{2,f} \lesssim 0.8\ M_\odot$). Rotational mixing could be important for (internally) more rapidly rotating stars, but only if thermohaline mixing is somehow rendered ineffective, or the accreted mass is only of the order of $10^{-3}\ M_\odot$. Then rotational mixing could lead to similar abundances as thermohaline mixing but gradually, over timescales comparable to the main sequence lifetime.

We find that in models with rotation velocities characteristic of CEMP-*s* stars ($2 \lesssim v_{\rm rot}$(km s^{-1}) $\lesssim 15$), rotational mixing suppresses the significant abundance anomalies (e.g. [C/Fe] < -1 from a post-mass-transfer abundance of [C/Fe] > 2) that in absence of rotation are expected to develop near the main sequence turn-off from uninhibited atomic diffusion (Matrozis & Stancliffe 2016). The models thus remain carbon-enhanced ([C/Fe] $\gtrsim 1$) throughout the evolution, as long as the rotation rates are high enough ($v_{\rm rot} \gtrsim 1$ km s^{-1}; Figs. 11, 14, 15). It is not known whether any CEMP-*s* (or in general metal-poor) stars rotate at still lower rates. But, if rotational mixing is indeed normally responsible for countering atomic diffusion in low-mass stars, such slowly rotating stars should have large abundance anomalies. These conclusions are rather insensitive to the parameters characterizing the efficiency of rotational mixing in our models (Fig. 18).

There is plenty of room for improvement in the treatment of angular momentum accretion and evolution. In particular, we

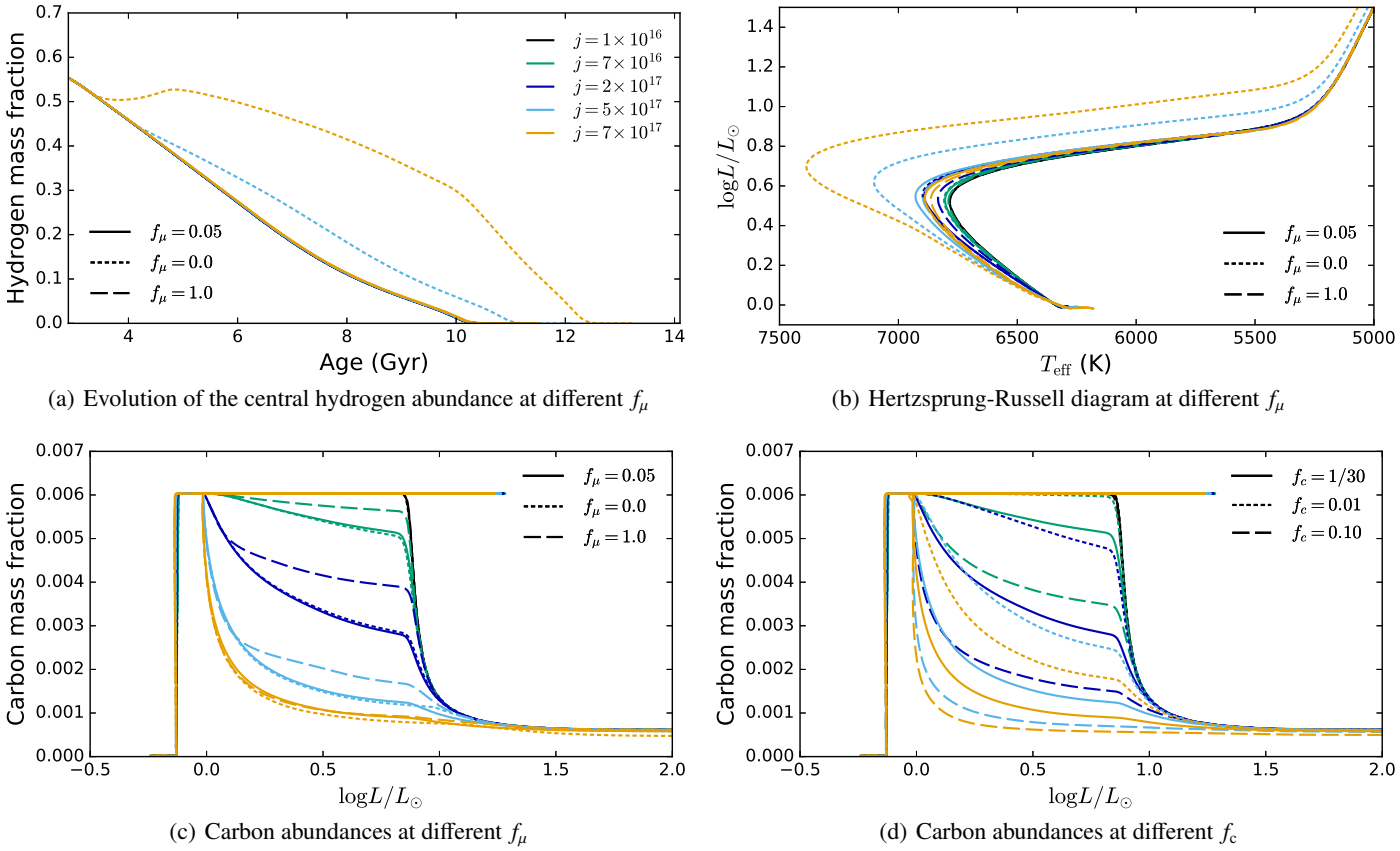

(a) Evolution of the central hydrogen abundance at different f_μ

(b) Hertzsprung-Russell diagram at different f_μ

(c) Carbon abundances at different f_μ

(d) Carbon abundances at different f_c

Fig. 17. Influence of changing the rotational mixing parameters f_μ (*panels a–c*) and f_c (*d*) in the system with $M_1 = 1.25\ M_\odot$, $M_{2,i} = 0.8\ M_\odot$, $\Delta M = 0.05\ M_\odot$. Models with rotational mixing only.

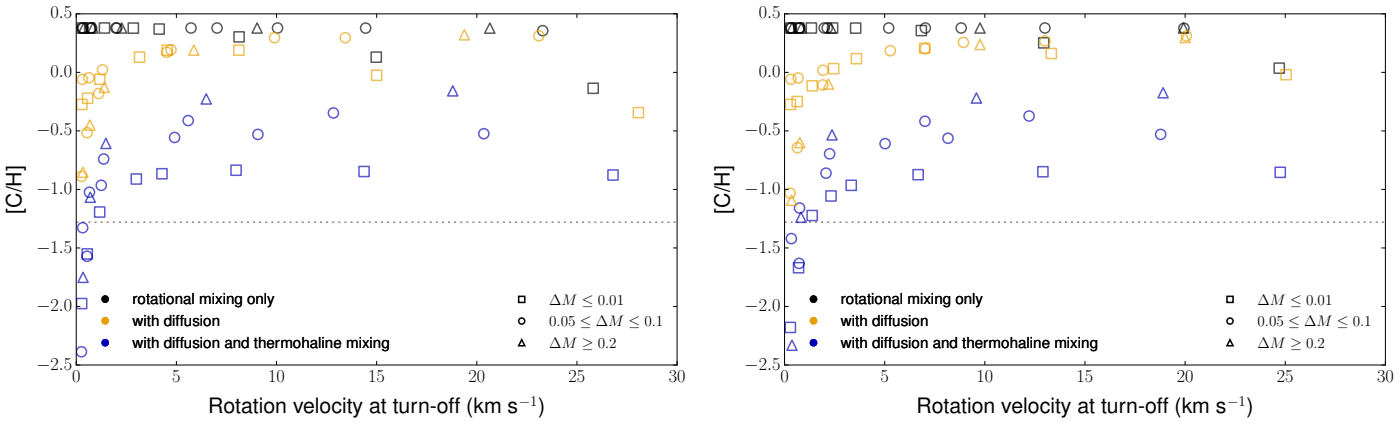

(a) f_μ = 1.0

(b) f_c = 0.01

Fig. 18. As Fig. 11 but with different values of f_c and f_μ.

have treated the ratio of angular momentum to mass accreted, i.e. the specific angular momentum of the accreted material, as a free parameter spanning three orders of magnitude. In real systems this range could be much more restricted, and dedicated multi-dimensional simulations are required to constrain it. Particularly, if the specific angular momentum is high, a mechanism for angular momentum loss during accretion must be identified. Otherwise, it is impossible to explain the most carbon-enhanced objects. Also, the nature and outcome of the mutual interaction between rotational and other instabilities, such as thermohaline convection, should be settled. Finally, we have only briefly considered the possibility of angular momentum loss following the mass transfer. But, since in terms of surface abundances such stars evolve similarly to more rapidly rotating stars without angular momentum losses, we do not expect this to invalidate our main conclusions.

Acknowledgements. We thank Adrian Potter for sharing his rotating version of the STARS code (RoSE) and Young Sun Lee and Timothy Beers for sharing the SDSS CEMP data. We also thank Carlo Abate for constructive comments on this manuscript. RJS is the recipient of a Sofja Kovalevskaja Award from the Alexander von Humboldt Foundation.

References

Abate, C., Pols, O. R., Izzard, R. G., & Karakas, A. I. 2015a, A&A, 581, A22
Abate, C., Pols, O. R., Karakas, A. I., & Izzard, R. G. 2015b, A&A, 576, A118
Abate, C., Pols, O. R., Stancliffe, R. J., et al. 2015c, A&A, 581, A62
Affer, L., Micela, G., Favata, F., & Flaccomio, E. 2012, MNRAS, 424, 11
Ahn, C. P., Alexandroff, R., Allende Prieto, C., et al. 2014, ApJS, 211, 17
Amard, L., Palacios, A., Charbonnel, C., Gallet, F., & Bouvier, J. 2016, A&A, 587, A105
Armitage, P. J., & Clarke, C. J. 1996, MNRAS, 280, 458
Asplund, M., Grevesse, N., Sauval, A. J., & Scott, P. 2009, ARA&A, 47, 481
Badnell, N. R., Bautista, M. A., Butler, K., et al. 2005, MNRAS, 360, 458
Beers, T. C., & Christlieb, N. 2005, ARA&A, 43, 531
Beers, T. C., Preston, G. W., & Shectman, S. A. 1985, AJ, 90, 2089
Bisterzo, S., Gallino, R., Straniero, O., Cristallo, S., & Käppeler, F. 2011, MNRAS, 418, 284
Bisterzo, S., Gallino, R., Straniero, O., Cristallo, S., & Käppeler, F. 2012, MNRAS, 422, 849
Bisterzo, S., Travaglio, C., Gallino, R., Wiescher, M., & Käppeler, F. 2014, ApJ, 787, 10
Böhm-Vitense, E. 1958, Z. Astrophys. 46, 108
Bouvier, J., Matt, S. P., Mohanty, S., et al. 2014, in Protostars and Planets VI (Tucson: University of Arizona Press), 433
Brandenburg, A., & Subramanian, K. 2005, Phys. Rep., 417, 1
Bressan, A., Marigo, P., Girardi, L., et al. 2012, MNRAS, 427, 127
Brott, I., de Mink, S. E., Cantiello, M., et al. 2011, A&A, 530, A115
Busso, M., Gallino, R., & Wasserburg, G. J. 1999, ARA&A, 37, 239
Cantiello, M., & Langer, N. 2010, A&A, 521, A9
Carollo, D., Beers, T. C., Bovy, J., et al. 2012, ApJ, 744, 195
Chaboyer, B., & Zahn, J.-P. 1992, A&A, 253, 173
Chaboyer, B., Demarque, P., & Pinsonneault, M. H. 1995a, ApJ, 441, 865
Chaboyer, B., Demarque, P., & Pinsonneault, M. H. 1995b, ApJ, 441, 876
Charbonneau, P. 2010, Liv. Rev. Sol. Phys., 7, 3
Charbonnel, C., & Lagarde, N. 2010, A&A, 522, A10
Chen, Z., Frank, A., Blackman, E. G., Nordhaus, J., & Carroll-Nellenback, J. 2017, MNRAS, 468, 4465
Christlieb, N., Green, P. J., Wisotzki, L., & Reimers, D. 2001, A&A, 375, 366
Cortés, C., Silva, J. R. P., Recio-Blanco, A., et al. 2009, ApJ, 704, 750
Deheuvels, S., Doğan, G., Goupil, M. J., et al. 2014, A&A, 564, A27
Denissenkov, P. A. 2010, ApJ, 723, 563
Denissenkov, P. A., & Pinsonneault, M. 2008a, ApJ, 684, 626
Denissenkov, P. A., & Pinsonneault, M. 2008b, ApJ, 679, 1541
Eggenberger, P., Meynet, G., Maeder, A., et al. 2010, A&A, 519, A116
Eggleton, P. P. 1971, MNRAS, 151, 351
Eggleton, P. P. 1972, MNRAS, 156, 361
Eggleton, P. P., Dearborn, D. S. P., & Lattanzio, J. C. 2006, Science, 314, 1580
Eldridge, J. J., & Tout, C. A. 2004, MNRAS, 348, 201
Endal, A. S., & Sofia, S. 1978, ApJ, 220, 279
Epstein, C. R., & Pinsonneault, M. H. 2014, ApJ, 780, 159
Fliegner, J., Langer, N., & Venn, K. A. 1996, A&A, 308, L13
Fricke, K. 1968, Z. Astrophys. 68, 317
Fuller, J., Lecoanet, D., Cantiello, M., & Brown, B. 2014, ApJ, 796, 17
Goldreich, P., & Schubert, G. 1967, ApJ, 150, 571
Hansen, T. T., Andersen, J., Nordström, B., et al. 2016, A&A, 588, A3
Heger, A., Langer, N., & Woosley, S. E. 2000, ApJ, 528, 368
Huarte-Espinosa, M., Carroll-Nellenback, J., Nordhaus, J., Frank, A., & Blackman, E. G. 2013, MNRAS, 433, 295
Iglesias, C. A., & Rogers, F. J. 1996, ApJ, 464, 943
Jorissen, A., Van Eck, S., Van Winckel, H., et al. 2016, A&A, 586, A158
Karakas, A. I. 2010, MNRAS, 403, 1413
Kawaler, S. D. 1987, PASP, 99, 1322
Kawaler, S. D. 1988, ApJ, 333, 236
Kippenhahn, R. 1974, in Late Stages of Stellar Evolution, eds. R. J. Tayler, & J. E. Hesser, IAU Symp., 66, 20
Kobayashi, C., Karakas, A. I., & Umeda, H. 2011, MNRAS, 414, 3231
Kraft, R. P. 1967, ApJ, 150, 551
Lee, Y. S., Beers, T. C., Masseron, T., et al. 2013, AJ, 146, 132
Liu, Z., Stancliffe, R. J., Abate, C., & Matrozis, E. 2017, ApJ, in press
Lucatello, S., & Gratton, R. G. 2003, A&A, 406, 691
Lucatello, S., Tsangarides, S., Beers, T. C., et al. 2005, ApJ, 625, 825
Lucatello, S., Beers, T. C., Christlieb, N., et al. 2006, ApJ, 652, L37
Lugaro, M., Karakas, A. I., Stancliffe, R. J., & Rijs, C. 2012, ApJ, 747, 2
Maeder, A., & Meynet, G. 2005, A&A, 440, 1041
Maeder, A., Meynet, G., Lagarde, N., & Charbonnel, C. 2013, A&A, 553, A1
Masseron, T., Johnson, J. A., Plez, B., et al. 2010, A&A, 509, A93
Masseron, T., Johnson, J. A., Lucatello, S., et al. 2012, ApJ, 751, 14
Matrozis, E., & Stancliffe, R. J. 2016, A&A, 592, A29
Matrozis, E., Abate, C., & Stancliffe, R. J. 2017, A&A, in press
Matt, S., & Pudritz, R. E. 2005a, ApJ, 632, L135
Matt, S., & Pudritz, R. E. 2005b, MNRAS, 356, 167
McClure, R. D., & Woodsworth, A. W. 1990, ApJ, 352, 709
McQuillan, A., Mazeh, T., & Aigrain, S. 2014, ApJS, 211, 24
Medrano, M., Garaud, P., & Stellmach, S. 2014, ApJ, 792, L30
Meibom, S., Barnes, S. A., Latham, D. W., et al. 2011, ApJ, 733, L9
Meibom, S., Barnes, S. A., Platais, I., et al. 2015, Nature, 517, 589
Mestel, L., & Spruit, H. C. 1987, MNRAS, 226, 57
Mosser, B., Goupil, M. J., Belkacem, K., et al. 2012, A&A, 548, A10
Noyes, R. W., Hartmann, L. W., Baliunas, S. L., Duncan, D. K., & Vaughan, A. H. 1984, ApJ, 279, 763
Pinsonneault, M. H., Kawaler, S. D., Sofia, S., & Demarque, P. 1989, ApJ, 338, 424
Pinsonneault, M. H., Deliyannis, C. P., & Demarque, P. 1991, ApJ, 367, 239
Placco, V. M., Frebel, A., Beers, T. C., & Stancliffe, R. J. 2014, ApJ, 797, 21
Pols, O. R., Tout, C. A., Eggleton, P. P., & Han, Z. 1995, MNRAS, 274, 964
Potter, A. T., Tout, C. A., & Brott, I. 2012a, MNRAS, 423, 1221
Potter, A. T., Tout, C. A., & Eldridge, J. J. 2012b, MNRAS, 419, 748
Sackmann, I. J. 1970, A&A, 8, 76
Schrijver, C. J. 1993, A&A, 269, 446
Seaton, M. J. 2007, MNRAS, 382, 245
Skumanich, A. 1972, ApJ, 171, 565
Spruit, H. C. 2002, A&A, 381, 923
Stancliffe, R. J., & Glebbeek, E. 2008, MNRAS, 389, 1828
Stancliffe, R. J., & Eldridge, J. J. 2009, MNRAS, 396, 1699
Stancliffe, R. J., Glebbeek, E., Izzard, R. G., & Pols, O. R. 2007, A&A, 464, L57
Stancliffe, R. J., Church, R. P., Angelou, G. C., & Lattanzio, J. C. 2009, MNRAS, 396, 2313
Starkenburg, E., Shetrone, M. D., McConnachie, A. W., & Venn, K. A. 2014, MNRAS, 441, 1217
Suda, T., Katsuta, Y., Yamada, S., et al. 2008, PASJ, 60, 1159
Suda, T., Yamada, S., Katsuta, Y., et al. 2011, MNRAS, 412, 843
Suda, T., Hidaka, J., Aoki, W., et al. 2017, PASJ, submitted [arXiv:1703.10009]
Suijs, M. P. L., Langer, N., Poelarends, A.-J., et al. 2008, A&A, 481, L87
Talon, S., & Charbonnel, C. 2003, A&A, 405, 1025
Talon, S., & Charbonnel, C. 2005, A&A, 440, 981
Talon, S., & Charbonnel, C. 2008, A&A, 482, 597
Theuns, T., Boffin, H. M. J., & Jorissen, A. 1996, MNRAS, 280, 1264
Travaglio, C., Galli, D., Gallino, R., et al. 1999, ApJ, 521, 691
Travaglio, C., Gallino, R., Busso, M., & Gratton, R. 2001, ApJ, 549, 346
Valenti, J. A., & Fischer, D. A. 2005, ApJS, 159, 141
VandenBerg, D. A., Richard, O., Michaud, G., & Richer, J. 2002, ApJ, 571, 487
Vauclair, S., & Théado, S. 2012, ApJ, 753, 49
Venn, K. A., Brooks, A. M., Lambert, D. L., et al. 2002, ApJ, 565, 571
Wasiutynski, J. 1946, Astrophysica Norvegica, 4, 1
Weber, E. J., & Davis, Jr., L. 1967, ApJ, 148, 217
Wehmeyer, B., Pignatari, M., & Thielemann, F.-K. 2015, MNRAS, 452, 1970
Yanny, B., Rockosi, C., Newberg, H. J., et al. 2009, AJ, 137, 4377
Yong, D., Norris, J. E., Bessell, M. S., et al. 2013, ApJ, 762, 27
Yoon, S.-C., Langer, N., & Norman, C. 2006, A&A, 460, 199
Zahn, J.-P. 1974, in Stellar Instability and Evolution, eds. P. Ledoux, A. Noels, & A. W. Rodgers, IAU Symp., 59, 185
Zahn, J.-P. 1992, A&A, 265, 115